Bulk actin dynamics drive phase segregation in zebrafish oocytes

Shayan Shamipour, Roland Kardos, Shi-Lei Xue, Björn Hof, Edouard Hannezo* and Carl-Philipp Heisenberg*
Institute of Science and Technology Austria, Klosterneuburg, Austria
*Correspondence: heisenberg@ist.ac.at and edouard.hannezo@ist.ac.at

SUMMARY

Segregation of maternal determinants within the oocyte constitutes the first step in embryo patterning. In zebrafish oocytes, extensive ooplasmic streaming leads to the segregation of ooplasm from yolk granules along the animal-vegetal axis of the oocyte. Here, we show that this process does not rely on cortical actin reorganization, as previously thought, but instead on a cell cycle-dependent bulk actin polymerization wave travelling from the animal to the vegetal pole of the oocyte. This wave functions in segregation by both pulling ooplasm animally and pushing yolk granules vegetally. Using biophysical experimentation and theory, we show that ooplasm pulling is mediated by bulk actin network flows exerting friction forces on the ooplasm, while yolk granule pushing is achieved by a mechanism closely resembling actin comet formation on yolk granules. Our study defines a novel role of cell cycle-controlled bulk actin polymerization waves in oocyte polarisation via ooplasmic segregation.

INTRODUCTION

Embryogenesis typically begins by reorganizing the cytoplasm within the oocyte (ooplasm). Seminal studies in tunicates have shown that the segregation of maternal determinants within the oocyte establish the blueprint for embryo patterning (Wilson 1900; Satoh 1994; Prodon, Sardet, and Nishida 2008; Prodon, Hanawa, and Nishida 2009; Nishida, Tokuhisa, and Muto 2017). Subsequent work in both vertebrate and invertebrate model organisms has demonstrated a common and essential role of ooplasmic reorganization for oocyte maturation and embryo patterning (Schuh and Ellenberg 2008; Nance, Munro, and Priess 2003; Nance and Zallen 2011).

However, the molecular and cellular mechanisms underlying ooplasm reorganization have only begun to be unravelled. Different cytoskeletal elements, and in particular the cortical actomyosin network, have been proposed to be involved (Sardet et al. 2007). In the nematode *Caenorhabditis elegans*, for instance, cortical actomyosin network flows are required for anterior-posterior polarization by accumulating cortex associated polarization cues at the anterior pole of the oocyte/zygote (Nance, Munro, and Priess 2003; Munro, Nance, and Priess 2004). Likewise in ascidians, cortical actomyosin flows are critical for germ layer specification by driving the segregation of maternal determinants within the oocyte (Prodon, Sardet, and Nishida 2008; Nishida, Tokuhisa, and Muto 2017). Finally, in starfish oocytes, periodic cortical actomyosin

contraction waves trigger ooplasm flows by dynamically changing oocyte shape (Klughammer et al. 2018). In addition to the cortical actomyosin network, the bulk actin cytoskeleton has also been implicated in ooplasm reorganization by positioning the nucleus and mitotic spindle during meiosis (Schuh 2011; Almonacid et al. 2015; Schuh and Ellenberg 2008; Azoury et al. 2008; Christine M. Field and Lénárt 2011). Yet, how the bulk actin cytoskeleton in regulated during these processes remains unclear.

Ooplasmic reorganization is particularly pronounced in oocytes from birds, reptiles, worms, and fish, containing a mixture of yolk granules (YGs) and ooplasm (Kostyuchenko and Dondua 2000; Abraham, Gupta, and Fluck 1993). Here, extensive ooplasmic streaming leads to the segregation of ooplasm from YGs with the ooplasm accumulating at the animal and YGs at the vegetal pole of the oocyte (Beams et al. 1985; Leung, Webb, and Miller 1998, 2000). Failure in ooplasm-YGs segregation leads to mislocalization of maternal determinants within the oocyte and subsequent defects in embryogenesis (Fuentes and Fernández 2010). Studies in both fish and worm oocytes have provided evidence that both the actin and microtubule cytoskeleton might play an important role in ooplasm-YGs segregation (Abraham, Gupta, and Fluck 1993; Shimizu 1999). In zebrafish oocytes, the prevalent model for ooplasm-YGs segregation suggests that ooplasmic streaming towards the animal pole is triggered by cortical actomyosin disassembly at the oocyte animal pole. This local weakening of the actomyosin cortex is thought to lead to a local expansion of the oocyte animal pole, which causes ooplasm to flow into this expansion (Beams et al. 1985; Leung, Webb, and Miller 1998, 2000; Fernández et al. 2006; Fuentes and Fernández 2010; Fuentes, Mullins, and Fernández 2018). While this appears to be a plausible model explaining ooplasm-YGs segregation, functional evidence supporting it is still lacking.

Here, we show that in zebrafish oocytes, the actomyosin cortex is dispensable for ooplasm-YGs segregation. Instead, this process is driven by cell cycle-dependent bulk actin dynamics. Cell-cycle entry triggers bulk polymerization waves travelling from the animal to the vegetal pole. These waves give rise to both contractility-driven F-actin flows, pulling the ooplasm via frictional drag towards the animal pole, and polymerization of comet-like F-actin structures, pushing YGs towards the vegetal pole.

RESULTS

Dynamics of ooplasm-yolk granules segregation

To determine how ooplasm segregates from YGs within the oocyte, we analyzed how the subcellular distribution of ooplasm and YGs changes during this process. Consistent with previous observations (Fernández et al. 2006; Fuentes and Fernández 2010), we found that shortly after egg activation, only a fraction of the ooplasm was found at the oocyte animal pole, while the remaining ooplasm was subdivided into multiple small pockets separated by YGs and distributed over the entire volume of the oocyte (Figure 1A). During the first 100 min after egg activation, nearly all of the ooplasm gradually accumulated at the animal pole of the oocyte, while the remaining part of the oocyte was filled with YGs only (Figure 1A; Movie 1). To understand how this segregation process is

dynamically regulated, we separately analyzed ooplasm and YGs movements along the oocyte AV axis during their segregation. By tracking the movements of ooplasm, marked by small fluorescent beads transplanted into the center of the oocyte, and YGs, marked by the expression of green-tagged version of Rac1 (Rac1-NGreen), we found that both ooplasm and YGs displayed periodic movements, which were tightly coupled to the cleavage cycle of the blastodisc (Figures 1B to 1F, Movies 2 and 3). Prior to each cleavage, ooplasm and centrally located YGs streamed animally, while YGs in more superficial/marginal regions of the oocyte moved vegetally (Figures 1C, 1E, 1F and 1G). During cytokinesis, these movements slowed down and partially reversed until the next cleavage cycle began. This suggests that ooplasm-YGs segregation is achieved by ooplasm and marginal YGs moving periodically and simultaneously in opposite directions, with the period of their movement being coupled to the cleavage cycle (Figures 1G and 1H).

Requirement of the actomyosin cortex for ooplasm-yolk granules segregation

Previous studies have put forward a model where ooplasm flows are generated by a pressure gradient along the oocyte AV axis due to a local expansion of the blastodisc that is caused by cortical actomyosin disassembly reducing blastodisc cortical tension (Beams et al. 1985; Fuentes, Mullins, and Fernández 2018; Leung, Webb, and Miller 1998, 2000). Consistent with this model, we found that cortical actin was periodically disassembled at the animal pole and that maxima of cortical disassembly precisely coincided with maxima of animal-directed ooplasm flows (Figure S1B). We also found that cortex disassembly at the animal pole led to reduced cortical tension and expansion of the blastodisc (Figures S1C to S1F).

To test whether this local modulation of cortical actomyosin within the oocyte is also needed for ooplasm-YGs segregation, we sought to interfere with this process and determine resultant effects on ooplasm flows. Consistent with previous observations (Leung, Webb, and Miller 2000), we found that global interference with actomyosin, but not microtubules, using drugs led to reduced velocities of both ooplasm and YGs flows and incomplete segregation (Figure S2; Movie 5). This suggests that actomyosin but not microtubules are required for proper ooplasm-YGs segregation.

To more specifically address the role of actomyosin cortex-mediated animal pole deformation for ooplasm-YGs segregation, we squeezed oocytes into cubic boxes to spatially confine them and thus prevent any animal pole expansion (Figure 2A, first row). Surprisingly, we found that periodic ooplasm flows still occurred in constrained oocytes, suggesting that animal pole expansion is dispensable for ooplasm to flow towards the animal pole (Figures 2A , 2B and 2C; Movie 6). To directly assess the role of the actomyosin cortex, we squeezed oocytes into cubic boxes and then broke their plasma membrane and underlying actomyosin cortex by strongly pushing the glass coverslip onto the boxed oocyte, thereby generating a mixture of YGs, ooplasm and highly fragmented pieces of cortex within a box (Figure 2A, second row). Remarkably, periodic, directed and coordinated ooplasm flows occurred in this ooplasm-YGs mixture, eventually leading to complete segregation of the ooplasm from the YGs (Figures 2A, 2B and 2C). This suggests that actomyosin cortex-mediated changes in oocyte shape are dispensable for ooplasm-YGs segregation.

Periodic actin polymerization waves regulated by the cleavage cycle oscillator

To search for alternative mechanisms driving ooplasm-YGs segregation, we asked whether actomyosin structures other than the cortex might be involved. Strikingly, we found actin periodically (de)polymerizing within the bulk of both 'cortex-free' (Figures 2D and 2E; Movie 7) and intact oocytes (Figure 2F; Movie 8) and that these periodic bulk actin polymerization events were inversely correlated with the periodic cortical actin (de)polymerization events reported previously (Figure 2G, Beams et al., 1985). We further found that bulk actin polymerization occurred in periodic waves travelling along the oocyte AV axis. These waves were initiated at the animal pole near the nucleus at the onset (metaphase) of the cleavage cycle coinciding with cortical actomyosin disassembly, and travelled towards the vegetal pole at an average velocity at its leading edge of about 50 $\mu m/min$ (Figures 2H and S3; Movie 9). Importantly, the onset of this bulk actin polymerization wave precisely coincided with the initiation of ooplasm flows (Figure 2I), pointing to the possibility that ooplasm-YGs segregation could be driven by periodic bulk actin polymerization waves travelling through the oocyte.

To test this possibility, we first asked how these waves are generated. Our observation that the period of the bulk actin polymerization wave was coinciding with the cleavage cycle and that actin polymerization waves occurred in metaphase, when Cdk1 activity is high, suggests that Cdk1 activity might be involved (Figures 3A, 3B and S4A; Movie 10). Previous work in *Xenopus* egg extracts and zebrafish blastula-stage embryos has suggested that the bulk actomyosin cytoskeleton undergoes regular, periodic pulses of gelation-contraction and that this process is cell cycle regulated (C. M. Field et al. 2011). Furthermore, recent studies in *Drosophila* embryos have identified trigger waves of Cdk1 activation travelling through the embryo during S phase (Deneke et al. 2016). We thus speculated that a similar Cdk1 wave might be responsible for the actin polymerization wave observed in the zebrafish oocyte. To test this hypothesis, we sought to change the frequency of the Cdk1 wave within the oocyte by interfering with the embryonic cell cycle oscillator (Tsai, Theriot, and Ferrell 2014). For reducing the frequency, we overexpressed Chk1 within the oocyte, previously shown to block a positive feedback loop (Deneke et al. 2016), or exposed oocytes to Dinaciclib to directly inhibit Cdk1 activity. For increasing the frequency, we exposed oocytes to the Wee1A inhibitor PD0166285, previously shown to block a negative feedback loop (Tsai, Theriot, and Ferrell 2014). We found that in Chk1 overexpressing or Dinaciclib-treated oocytes, the frequency of the bulk actin polymerization wave was decreased, while in oocytes treated with PD0166285, the frequency was increased (Figures 3C and 3D). Furthermore, these changes in the frequencies of the bulk actin polymerization waves were accompanied by similar changes in the frequencies of ooplasm flows and YGs movements, suggesting that these processes are coupled (Figures 3E, S4B and S4C). This supports the hypothesis that Cdk1 waves drive the observed bulk actin polymerization waves and that these waves regulate ooplasm flows.

To investigate whether the Cdk1 wave can spontaneously self-organize within the ooplasm of the blastodisc independently of the nucleus, we cut an S phase oocyte (at around 10 min post fertilization (mpf)) perpendicular to its AV axis, thereby generating an animal half mini-oocyte containing the blastodisc and some of the YGs, and a vegetal half mini-oocyte containing most of the YGs and some ooplasm pockets. Strikingly, we observed that both animal and vegetal half

mini-oocytes were able to generate bulk actin polymerization waves and that these waves triggered efficient ooplasm-YGs segregation (Figure 3F; Movie 11). This suggests that these waves can spontaneously emerge within the ooplasm independently from the nucleus and blastodisc. However, we also noticed that the vegetal half mini-oocytes started actin polymerization in average 10 min later than the animal half mini-oocytes (Figures 3G and 3H), a delay significantly larger than expected for the time needed for the Cdk1 wave to propagate from the animal to the vegetal pole (~ 6 min). Such de-synchronization after physical separation is a hallmark of trigger waves, suggesting that the observed actin polymerization waves in metaphase are synchronized by Cdk1 trigger waves during S phase.

Contractility-driven actin network flows during ooplasm-yolk granules segregation

To understand how the bulk actomyosin wave might drive ooplasm-YGs segregation, we examined the organization of the bulk actin network along the oocyte AV axis prior and during wave formation (Figures 4A, 4A' and S5A). We found that prior to the first wave, the bulk actin network displayed a graded distribution along the AV axis with its highest level at the animal pole and that during actin wave propagation this gradient was further enhanced (Figure 4A'). Gradients of contractile actomyosin networks have previously been suggested to have the potential of triggering actin flows (Mayer et al. 2010; Munro, Nance, and Priess 2004; Munjal and Lecuit 2014). We thus speculated that the observed AV actin gradient might trigger animally directed actin flows (Figure 4B). To test this hypothesis, we examined bulk actin network dynamics during wave propagation at high spatiotemporal resolution (Figure 4C; Movie 12). We observed that, upon wave initiation, a dense filamentous actin network polymerized within the bulk, with its maximum intensity remaining at the animal pole while the wave was propagating vegetally (Figures 4C and 4C'). Strikingly, Particle Image Velocimetry (PIV) and kymograph analyses revealed that while the polymerization wave kinematically propagated vegetally, actin filaments were advected in the opposite direction towards the peak of actin intensity at the animal pole (Figures 4D ,4D' and S5B). Given the importance of actomyosin tension for actin flows and the co-localization of Myosin-2 with F-actin in the bulk actin network (Figure S5C; Movie 13), we asked whether the bulk F-actin network indeed displays tension along the oocyte AV axis when flowing. For probing tension, we performed laser-cuts of the bulk F-actin network before and during the flows. While we did not observe any recognizable tension before the F-actin flows began (Figure S5D), the network tension along the AV axis of the oocyte sharply increased when bulk F-actin flows set in (Figures 4E, 4F, S5E and S5E'). This strongly suggests that the bulk actin polymerization waves generate a gradient of filamentous actin along the oocyte AV axis, which gives rise to periodic tension-driven bulk F-actin flows towards the animal pole.

Function of contractility-driven actin network flows in ooplasm-yolk granules segregation

The synchrony between bulk F-actin flows and ooplasm-YGs segregation points to the possibility that these two processes are causally related. For instance, F-actin flows might drag ooplasm more than YGs via passive frictional forces, thereby segregating these two phases. To address this possibility, we developed a generic three-component (actin, ooplasm and YGs) porous medium description of the oocyte (for details see Methods), using the classical theory of active gels for the actomyosin phase (Prost, Jülicher, and Joanny 2015), and a poro-viscous theory for the mixture of

ooplasm and YGs, where each phase interacts with each other via passive frictional forces (Mogilner and Manhart 2018). Briefly, the model consists of

(i) conservation equations for the fraction ϕ_i of each of the three phases (F-actin, ooplasm and YGs, with respective subscripts i=*a*, *o* and *y*), which can change due to advective velocities v_i and a polymerization rate *R* for F-actin:

$$\partial_t \phi_a + \nabla(v_a \phi_a) = R$$
$$\partial_t \phi_o + \nabla(v_o \phi_o) = 0$$
$$\partial_t \phi_y + \nabla(v_y \phi_y) = 0$$

(ii) force balance on each phase *i*, which is in frictional contact with the other two phases *j* with corresponding force $\phi_i \phi_j \xi_{ij}(v_i - v_j)$, proportional to their local difference in velocity and relative friction coefficient ξ_{ij};

(iii) constitutive equations for the rheological behavior of each of the three phases. The ooplasm and YGs were taken as simple fluids of viscosity η_o and η_y, while the rheology of F-actin was described by the aforementioned active gel theory $\sigma_a = \eta_a \nabla v_a + \chi \phi_a$, where σ_a is the stress in the F-actin gel, χ its isotropic active contractility and η_a its viscosity.

To gain insight into the qualitative features of the resulting dynamics, we first studied a one-dimensional scenario, considering the effect of a given F-actin flow on the ooplasm and YGs phases (Mogilner and Manhart 2018). Importantly, the relative magnitude of the actomyosin-ooplasm and actomyosin-YGs friction coefficients (ξ_{ao} and ξ_{ay}, respectively) was found to play a crucial role in the resulting dynamics in this 3-component description: if both coefficients are the same, a given actin flow v_a does not lead to any net flow of ooplasm and YGs ($v_o = v_y = 0$) due to incompressibility constraints (for details see Methods, Figure 5B). In contrast, if the friction coefficients are different, then a relative velocity sets in between the two phases, whose sign and magnitude is dictated by the relative difference in friction coefficients:

$$v_o \propto v_a (\xi_{ao} - \xi_{ay})$$

For ooplasm and not YGs, to be dragged along with F-actin, its frictional interaction with actin would thus need to be the strongest (Figures 5A and 5B). To test this hypothesis, we experimentally estimated the friction coefficients between the phases. The characteristic drag coefficient ξ experienced by a moving fluid of viscosity η permeating a network with characteristic mesh/pore size of d_{mesh} can be estimated by the classical relationship $\xi = \frac{\eta}{d^2_{mesh}}$ (neglecting pre-factors from the detailed structure of the porous media). Therefore, the characteristic actin-ooplasm and actin-YGs drag coefficients can be estimated as $\xi_{ao} = \frac{\eta_o}{d^2_{F-actin}}$ and $\xi_{ay} = \frac{\eta_a}{d^2_{granules}}$, respectively, with η_o and η_a being ooplasm and F-actin viscosities. To this end, we measured the viscosity of bulk actomyosin network through pipette aspiration, and the viscosity of the ooplasm via microrheology (Figures S5F, S5F', S5G, S5GF' and S5G''; for details see Methods). We found $\eta_o \approx 20$ mPa.s and $\eta_a \approx 40$ Pa.s, consistent with previous measurements in zebrafish, *Xenopus* and *Drosophila* embryos (C.-C. Chang et al. 2012; Monteith et al. 2016; Valentine et al. 2005). Moreover, the characteristic mesh-size of the

actomyosin cytoskeleton is typically ~50-100 nm, (Charras et al. 2005; Keren et al. 2009), while the pore-size that we measured for the YGs phase is 2-3 orders of magnitude larger ($d \approx 15\ \mu m$, Figure S5H). This difference in pore/mesh size means that local viscous flow gradients are much sharper between actin and ooplasm than between actin and YGs, and, consequently, that actin-ooplasm friction is conservatively at least an order of magnitude larger than actin-YGs friction ($\xi_{ao} >> \xi_{ay}$, for details see Methods, Figure 5A). This differential friction then predicts that F-actin and ooplasm flows should have similar magnitude and directionality, while YGs should flow in the opposite direction, leading to phase segregation. Consistent with this, we measured F-actin and ooplasm flow velocity in time and found that they were tightly correlated both in terms of their temporal dynamics and flow amplitudes (Figure 5C).

Generation and directionality of F-actin flows within the oocyte

While our analysis so far suggests that directional F-actin flows might be sufficient for ooplasm-YGs segregation within the oocyte, questions remain as to the generation and directionality of those flows. Given the higher actin concentration observed at the animal pole at the onset of the bulk actin polymerization wave (Figures 4A and 4A'), we speculated that this unequal actin distribution biases the directionality of flows. To address this possibility, we compared theoretical and experimental F-actin flows within the oocyte (Figures 5D and 5F) based on the experimentally observed F-actin distribution within the oocyte at the onset of wave propagation. Interestingly, we found a close match between the predicted and observed F-actin flow profiles with the peak flow velocity coinciding with the point where the F-actin intensity gradient is largest (Figures 5D and 5F). To further challenge the model, we sought to interfere with two critical features of F-actin flow generation: Myosin-2 dependent actin network contractility being essential for F-actin flows, and unequal F-actin and/or Myosin-2 distribution polarizing these flows. For interfering with actomyosin network contractility, we overexpressed CAMypt within the oocyte, an approach that led to incomplete ooplasm-YGs segregation (Figure S2). As predicted by our model, we found that in CAMypt-overexpressing oocytes, bulk F-actin flows towards the animal pole were strongly diminished (Figures 5E, 5G and 5G'). Notably, we also observed that ooplasm and F-actin flow velocities were reduced by similar amounts in CAMypt-overexpressing oocytes (Figure 5H), consistent with the model prediction that F-actin drags along ooplasm while moving towards the animal pole.

For evaluating how changes in the distribution of F-actin and/or Myosin-2 within the oocyte affect F-actin flows, we first attempted to recapitulate the overall dynamics of the segregation process with our 1D model using different strength of pre-patterned F-actin gradients. By systematically exploring the parameter space, we found that the experimentally observed steepness of the pre-patterned F-actin gradient was theoretically sufficient to robustly direct flows towards the animal pole of the oocyte (Figures S6A, S6B, 6A and 6B; for details see Methods). Moreover, we found that the theory could explain several other features of the experimental data, such as the characteristic exponentially decreasing profile of the ooplasm away from the animal pole (Figure S5J, see Supplementary Theory for details), and the complex merging dynamics of ooplasm pockets throughout ooplasm-YGs phase segregation, where the ooplasm close to the animal pole is rapidly

advected towards the animal pole, while ooplasm further away from the animal pole coarse-grains and requires several movement cycles to fully segregate (Figures 6A, 6B, S6C and S6C'). This supports the plausibility of our assumption that the pre-patterned gradient of actin within the oocyte drives F-actin flows towards the animal pole.

Secondly, a key prediction of our model is that in the absence of a pre-patterned F-actin gradient, ooplasm-YGs phase segregation would still occur because of a self-reinforcing contractile instability, but in a mislocalized manner, with ooplasm accumulating in the center rather than at the animal pole of the oocyte (Figures 6C, S6D and Supplementary Theory for details). To experimentally test this, we sought to interfere with the pre-patterned F-actin gradient within the oocyte by treating oocytes with Cytochalasin B (CytoB) or Jasplakinolide (Jasp) to block F-actin assembly or stabilize F-actin, respectively. We observed that in both CytoB and Jasp-treated oocytes, the global AV actin gradient was significantly reduced, whereas bulk F-actin levels in the center of the egg were left unchanged (Figure 6D). Strikingly, we also found that treated oocytes displayed periodic and radial flows of F-actin towards their center and that these radial flows led to the formation of large ooplasmic pockets in the egg center (Figure 6E; Movie 14). This confirmed our model prediction that the occurrence of F-actin flows is independent of any prior guiding cues and that the resultant macroscopic ooplasm-YGs phase segregation can be decoupled from its localization. Furthermore, simulating the detailed dynamics of ooplasm-YGs segregation using the same model as for control oocytes but without a pre-patterned F-actin gradient, yielded results that closely matched the phase segregation process observed in CytoB and Jasp-treated oocytes, with actin waves driving gradual coalescence of nearby ooplasm-enriched zones until a single accumulation remained in the center of the oocyte (Figures 6F and S6D'). Notably, the effect of Jasp on gradient reduction was generally weaker than of CytoB, which was accompanied by a weaker ooplasmic mislocalization phenotype (Figures 6D and S6E), also in agreement with the model prediction (Figure S6A). Collectively, these findings support our model prediction that pre-patterned F-actin gradients within the oocyte are instructive for the directionality of self-organized F-actin/ooplasm flows and thus ooplasm-YGs segregation.

Actin comet formation in ooplasm-yolk granules segregation

While the F-actin flow-mediated pulling mechanism via differential friction described so far can explain the ooplasm-YGs segregation behavior in a one-dimensional setting, the dynamic shape changes of blastodisc-to-YGs interface (BYI) and the complex two-dimensional swirling patterns of YGs remained to be explored. To test whether this could be captured by our model, we extended the model to 2D simulations taking into account egg geometry and a stress-free BYI (for details see Methods). These simulations could accurately reproduce the observed swirling motion of YGs when assuming that a larger frictional force is exerted on the granules in the center of the oocyte, an assumption justified by our observation that the fluid fractions, and thus F-actin, are initially higher in the center (Figure S7A). Such swirling motion, however, also implies that YGs in central portions of the BYI move animally (Figure 7A). Consequently, the BYI will take on an increasingly bulged shape during the segregation process, which could potentially pose a problem for ooplasm-YGs segregation by allowing YGs to move back into the blastodisc. To test this prediction experimentally, we analyzed BYI shape changes during the first two bulk actin polymerization waves (Figure 7B;

Movie 15). This analysis showed that the BYI indeed became more bulged towards the end of the first polymerization wave (Figures 7B, 7C and S7B). However - and not predicted by our 2D simulations - it also showed that this interface straightened again at the onset of the second polymerization wave, with YGs in the center of the BYI moving vegetally (Figures 7B, C and S7C). This biphasic behavior of the BYI bending-up during and towards the end of F-actin/ooplasm flows (protruding phase) and straightening shortly before the next round of flows was initiated (straightening phase), was repeated during the first 3-4 cleavages, suggesting that they are an inherent feature of the segregation process (Figure S7C).

To understand this, we analyzed how actin might specifically interact with the BYI at initial stages of bulk actin wave formation. Strikingly, we found that during wave propagation, actin polymerized on the surface of YGs (Figures 7D and 7D'; Movie 16). Analyzing actin polymerization on YGs at high spatiotemporal resolution showed that actin polymerized predominantly where YGs were in contact with ooplasm (Figures 7D'', S7D and S7D'). As this interface is most prominent at the BYI (Figure 7D''), actin predominantly polymerized there. Coinciding with actin polymerization on their surface, YGs at the BYI deformed into a pear shape and began to move downwards towards the vegetal pole in a direction opposite to their site of actin polymerization, thereby straightening the BYI (Figure 7E-G; Movie 17). The polymerized actin typically remained associated with the granules and followed them as they moved vegetally (Figure 7F), suggesting that their movements are interlinked. To further test this possibility, we transplanted YGs from a donor oocyte into the blastodisc of a host oocyte prior to bulk actin polymerization wave formation (Figure S7F; Movie 18). When the bulk actin polymerization wave was initiated at the animal pole of the oocyte, actin polymerized on the animal side of the transplanted YGs where they faced the blastodisc, followed by the transplanted granules moving vegetally (Figures S7F and S7F'). Interestingly, we also found that small YGs dispersed within the ooplasm-filled blastodisc formed actin comet-like structures and became highly motile once the actin polymerization wave started to form at the animal pole (Figure 7H; Movie 19). This behavior was highly reminiscent of the previously described comet-driven movement of the intracellular pathogen *Listeria monocytogenes* (Theriot et al. 1992) and of protein-coated beads and vesicles (Cameron et al. 1999; Giardini, Fletcher, and Theriot 2003; Bernheim-Groswasser, Prost, and Sykes 2005; Plastino and Sykes 2005). To test whether actin polymerization on YGs is regulated by the same factors as found for actin comet formation, we exposed oocytes to inhibitors of the actin nucleators Arp2/3 and Formin, previously implicated in comet formation (Jermy 2010; Miao et al., n.d.; Borinskaya et al. 2016). Interestingly, we found that inhibition of Formin, but not Arp2/3, strongly reduced actin polymerization on YGs, suggesting that actin polymerization on YGs shares some but not all regulators of actin comet formation (Figures S7E and S7E').

Our observation of actin comet formation at the BYI suggests that this might act as a corset on YGs at the BYI, effectively rigidifying the interface to prevent the YGs from moving back into the blastodisc. To test this hypothesis, we extended our numerical simulation of the segregation process by considering that actin-polymerization at the BYI imposes zero-relative speed (instead of zero stress) for YGs (for details see Methods). Simulations with this extended 2D version of our hydrodynamic model provided a more realistic description of our experimental observations of YGs

movements during the straightening phases (Figures 7I and 7I'). Collectively, these combined experimental and theoretical observations point to the possibility that actin comet formation on YGs at the BYI might work in concert with actin flows in efficiently segregating ooplasm from YGs (Figure S7G).

Next, we searched for conditions where this process was specifically impaired. Recent studies have shown that in oocytes mutant for the atypical cadherin *dachsous (dchs)*, known to regulate the actin cytoskeleton, ooplasm-YGs segregation is defective (Li-Villarreal et al. 2016). Closer inspection of *dchs* mutant oocytes revealed that actin comet formation on YGs at the BYI was specifically impaired (Figures 7J and 7K; Movie 20), while bulk F-actin dynamics within the oocyte appeared largely unchanged (Figure 7L). Interestingly, in the absence of actin comet formation in *dchs* mutant oocytes, we found that - although ooplasm-YGs phase segregation still occurred in the bulk of the oocyte (Figure S7H; Movie 21) - central YGs close to the animal pole were ectopically flowing together with the ooplasm and actin into the blastodisc (Figures 7J and S7H). This led to a highly irregular BYI, as expected theoretically for a stress-free interface (Figures 7I). Collectively, these observations suggest that Dchs-dependent actin comet formation on YGs at the BYI effectively rigidifies the interface to refine ooplasm-YGs phase segregation and prevent local inter-mixing of YGs with ooplasm.

DISCUSSION

Our data suggest that the segregation of ooplasm from YGs along the AV axis of the zebrafish oocyte depends on the concerted activities of two distinct force generating mechanisms exerted by the bulk actomyosin cytoskeleton within the oocyte: pulling forces generated by contraction and flow of the bulk actomyosin network that passively drag ooplasm towards the animal pole via differential friction, and pushing forces generated by actin comets on the surface of the YGs that move YGs towards the vegetal pole. Previous studies in zebrafish have proposed that the disassembly of the actomyosin cortex at the animal pole drives ooplasm flow and segregation by triggering shape changes of the oocyte (Beams et al. 1985). Our data, in contrast, show that the actomyosin cortex of the oocyte is dispensable for this process and that, instead, the bulk actin network provides the main force-generating activity driving ooplasm-YGs segregation.

A key finding of our study is that bulk actomyosin flows, previously implicated in a wide variety of processes (Mayer et al. 2010; Munro, Nance, and Priess 2004; Munjal and Lecuit 2014), function as the prime force-generating process triggering ooplasm-YGs segregation, thereby identifying a yet unknown role for them in phase segregation. Importantly, our results suggest that phase segregation results from the differential frictional interaction of bulk actomyosin networks with ooplasm and YGs. Moreover, we show that this segregation process is controlled by a combination of self-organizing properties inherent for self-amplifying contractility-driven flows and pre-patterned cues given by the graded distribution of actin along the oocyte AV axis. The theory we developed to describe this process recapitulates major features of the segregation process and is generic to any setting of cytoskeletal flows in biphasic mixtures.

Our study further demonstrates that the bulk actomyosin network functions also by generating pushing forces on YGs through actin comet formation. Actin comet formation and function have been extensively studied in the context of bacteria motility (Theriot et al. 1992; Egile et al. 1999). Studies using polystyrene beads coated with actin nucleation promoting factors have provided insight into the molecular and biophysical mechanisms by which actin comets form and function in bacterial cell motility (Bernheim-Groswasser et al. 2002). Interestingly, actin comets have also been observed to form in a cell cycle-dependent manner on endocytic vesicles within early *Caenorhabditis elegans* and zebrafish embryos, although the functional relevance of this remains unclear (Velarde, Gunsalus, and Piano 2007; C. M. Field et al. 2011). By showing that actin comet formation is required for proper ooplasm-YGs segregation, our study provides evidence for a novel function of actin comets in development.

The molecular, cellular and biophysical basis of cytoplasmic flows have only begun to be unravelled. Our findings identify an important function of cell-cycle dependent periodic pulses of bulk actin gelation-contraction in this process. Studies in *Xenopus* egg extracts have shown that the bulk actomyosin network undergoes regular, periodic pulses of gelation-contraction and that this behavior is controlled by the cleavage cell cycle regulating F-actin nucleation (J. B. Chang and Ferrell 2013). This is strikingly similar to our observation of periodic bulk actin polymerization waves within zebrafish oocytes mediated by a trigger wave of Cdk1, suggesting that the generation of Cdk1 waves might represent a common and evolutionary conserved mechanism of how to regulate actomyosin activity on the scale of oocytes and embryos, where diffusion will be too slow to efficiently modulate actomyosin.

Yet, how the cell cycle machinery controls cytoskeletal organization remains poorly understood. Cdk1 and Chk1 have recently been proposed to regulate each other via a double negative feedback loop that can on its own give rise to cell cycle wave propagation (Deneke et al. 2016), and to modulate cortical actomyosin contractility by influencing RhoA activity (Matthews et al. 2012; Ramanathan et al. 2015)(Bischof et al., n.d.; Royou, Sullivan, and Karess 2002)(Matthews et al. 2012; Ramanathan et al. 2015). Moreover, the actomyosin cytoskeleton can give rise to self-organized flows and patterns arising purely from its mechanical properties (Prost, Jülicher, and Joanny 2015; Hannezo et al. 2015). Still, how both of these processes spatiotemporally communicate with each other remains largely unknown. Our findings provide a first step towards an integrated understanding of the mechanochemical feedback loops between cell cycle regulators and cytoskeletal dynamics.

ACKNOWLEDGMENTS

We would like to thank Guillaume Salbreux and Silvia Grigolon for advice on the theory, Lila Solnica-Krezel for kindly providing us with zebrafish *dachsous* mutants, members of the Heisenberg and Hannezo groups for fruitful discussions, and the Bioimaging and zebrafish facilities at IST Austria for their continuous support. This project has received funding from the European Union

(European Research Council Advanced Grant 742573) to C.P.H, and from the Austrian Science Fund (FWF) [P 31639] to E.H.

AUTHOR CONTRIBUTIONS

S.S. and C.-P.H. designed the research. S.S. performed the experiments and analyzed the experimental data. R.K. created *Tg(actb1:mNeonGreen-Rac1a)* zebrafish line. S.-L.X. and E.H. performed the modelling and numerical simulations. S.S., B.H., E.H. and C.-P.H. wrote the manuscript.

DECLARATION OF INTERESTS

The authors declare no competing interests.

FIGURE LEGENDS

Figure 1. Dynamics of ooplasm-yolk granules segregation.
(**A**) Bright-field (upper row) and fluorescence (Dextran labeling the ooplasm, lower row) images of zebrafish oocytes from 30 to 70 min post fertilization (mpf). AP, animal pole; and VP vegetal pole. (**B**) Images of oocytes injected with Dextran (Magenta) and beads (red, 2 μm) to mark ooplasm flows. (**C**) Averaged speed of injected beads during the first 100 mpf. Green dashed lines mark the first 4 cleavages. N=3 experiments, n=7 oocytes. (**D**) Images of oocytes expressing Rac1-NGreen to mark ooplasm and yolk granules (YGs, upper row), YGs segmented from the images above (middle row), and Particle Image Velocimetry (PIV) analysis of YG movements (lower row; + velocities, animalwards; - velocities, vegetalwards). Dashed line in left panel middle row marks lateral axis of the oocyte. (**E, F**) Kymograph of YGs velocity along the animal-vegetal (AV, E) and lateral axes of the oocyte (F) as a function of time. Velocity is color-coded as in (D). (**G**) Average flow speed of central and marginal YGs (red and blue) and ooplasm (green) over time. Ooplasm flows were measured by segmenting the ooplasm from Rac1-NGreen expressing oocytes and performing PIV. N=3, n=7. (**H**) Schematic illustrating ooplasm and YG flow patterns in the oocyte. Error bars, SEM.

Figure 2. Requirement of the actomyosin cortex for ooplasm-yolk granules segregation and spatiotemporal correlation between ooplasm flows and periodic bulk actomyosin waves.
(**A**) Images of oocytes injected with beads (red) to mark ooplasm flows. Intact oocytes (upper row) and oocytes with fragmented actomyosin cortex ('cortex-free', lower row) confined in squared-shaped boxes. (**B,C**) Averaged speed (B) and distance from the animal pole (C, normalized to the AV axis) of injected beads in unconfined control (blue, N=1 experiment, n=3 oocytes), confined (red; N=3, n=5) and confined & cortex-free oocytes (green; N=3, n=3). (**D**) Images of cortex-free oocytes expressing Utr-GFP to mark F-actin. (**E**) Normalized bulk actin intensity of cortex-free oocytes during the first 100 min post fertilization (mpf). N=1, n=3. (**F**) Images of F-actin in the blastodisc of oocytes. (**G**) Normalized bulk (red, left axis, N=1, n=3) and cortical (blue, right axis, N=1, n=4) actin intensity during the first 100 mpf. (**H**) Images of F-actin in oocytes. Blue point in left panel marks the centre of the bulk actin polymerization wave. Dashed line outlines the boundary of the bulk actin polymerization wave. (**I**) Averaged bulk actin intensity (red, left axis) and flow speed (blue, right axis) during the first 100 mpf. N=1, n=3. Error bars, SEM.

Figure 3. Regulation of periodic actin polymerization waves by the cleavage cycle oscillator.
(**A**) Images of the blastodisc of oocytes expressing DCLK-GFP and Utr-mCherry to mark microtubules and F-actin, during the first cell cycle. (**B**) Schematic illustrating the embryonic cell cycle oscillator and its regulation of bulk actin polymerization. (**C**) Normalized bulk actin intensity in control (blue, N=1 experiment, n=2 oocytes, measured on 5 different stacks: z=5), Wee1 inhibitor treated (red, N=1, n=2, z=6), Chk1 overexpressing (Chk1-OE, green, N=1, n=2, z=10) and Cdk1 inhibitor treated (black, N=2, n=6, z=6) oocytes during the first 100 mpf. (**D**) Periodicity of bulk actin oscillations for the conditions described in (C). *$P=0.0253$, ** $P=0.0095$, **** $P<0.001$, Unpaired t-test. (**E**) Periodicity of bulk actin oscillations (same data as in (C)) and YGs movements

for the conditions described in (C). For YG movements: Control (N=2, n=6), Wee1 inhibitor (N=2, n=4), Chk1-OE (N=2, n=8), Cdk1 inhibitor (N=2, n=4). (**F**) Images of mini-oocytes marking F-actin, obtained from the animal (A) half (upper row) or vegetal (V) half (lower row) of an oocyte. Panels boxed in gold correspond to the onset of the bulk actin polymerization wave. (**G**) Normalised bulk actin intensity in the A (red) and V (blue) mini-oocytes during the first 100 mpf. N=1, n=3 for each case. (**H**) Onset of bulk actin polymerization waves in A and V mini-oocytes, their onset delay, and expected delay calculated from the speed of the polymerization wave as shown in (Figure S3C). Box and Whiskers, min to max. N=4, n=13 (for each A and V mini-oocytes) . **** P <0.001, Mann-Whitney test. Error bars, SEM except in (E), SD.

Figure 4. Contractility-driven actin network flows during ooplasm-yolk granules segregation
(**A**) Images of oocytes expressing Utr-GFP to mark F-actin. The yellow ROIs indicate ooplasmic pockets across the oocyte, where actin intensity was measured in (A'). (**A'**) Normalized intensity of the bulk actin within the ooplasm along the oocyte animal-vegetal (AV) axis prior to (cyan) and during (magenta) bulk actin polymerization wave. N=4 experiments, n=7 oocytes. ***** P <0.001,* ns: not significant, Mann-Whitney test. (**B**) Schematic illustrating the vegetalward movement of the bulk actin polymerization wave (green) and animalward flows of bulk actin (red) along the actin gradient shown in (A'). (**C**) High magnification images of marginal regions of the oocyte marking F-actin. (**C'**) Kymograph of actin intensity observed in (C) along the AV axis as a function of time. White dashed line outlines the boundary of the bulk actin polymerization wave. Hot-to-cold color coding corresponds to high-to-low actin intensity. (**D**) Particle Image Velocimetry (PIV) analysis of F-actin flows in the regions of the oocyte shown in (C). Color code ranges from high (red) to low absolute velocities (blue). (**D'**) Kymograph of actin velocities along the AV axis of the oocyte as a function of time. Velocity is color coded as in (D). (**E**) Images of oocytes marking F-actin during bulk actin network laser ablation. Yellow dashed line, laser ablation site. Arrowheads outline recoil of the actin network around the cut. (**F**) Recoil distance of the cut actin network prior (red, N=3, n=15) and during (blue, N=5, n=13) bulk actin polymerization wave, calculated from kymographs as shown in (Figures S5D and S5E). Error bars, SEM.

Figure 5. Function of contractility-driven actin network flows in ooplasm-yolk granules segregation.
(**A**) Schematic illustrating the friction forces exerted by the flowing bulk actin network (v_a) on YGs (f_{ay} , centre, blue arrows) and the ooplasm (f_{ao} , right, green arrow). $d_{yg\ mesh}$ and $d_{actin\ mesh}$ indicate the mesh size of YGs and bulk actin, respectively. Light green area in the microscopic scale indicates the area experiencing the friction induced by actin on the ooplasm. (**B**) Predicted relative velocities of ooplasm to actin (V_o/V_a) as a function of the relative friction coefficients (ξ_{ao}/ξ_{ay}) according to the 1D active gel model. For large (or small) ξ_{ao}/ξ_{ay} , F-actin and ooplasm (or F-actin and YGs) velocities become similar, resulting in ooplasm (o) (or YGs (y)) accumulation at the animal side of the oocyte. (**C**) Ooplasm (N=3 experiments, n=7 oocytes) and F-actin (N=3, n=3) flow velocity during the peak of the first bulk actin polymerization wave. Ooplasm and bulk actin flow velocity values were obtained from (Figures 1G and 4D), respectively. (**D**) Predicted F-actin intensity and velocity profiles along the animal-vegetal (AV) oocyte axis, as a result of increased actomyosin

contractility at the animal pole (AP, shadowed area), showing a peak of F-actin velocity towards the AP where the F-actin gradient is steepest. (**E**) Predicted F-actin velocity in oocytes with uniformly reduced actomyosin contractility by 40% (green, simulating the experimental CAMypt condition) compared to unchanged contractility values (blue, resembling WT). (**F**) Averaged F-actin intensity (red, left axis) and flow velocity (blue, right axis) along the AV axis of the oocyte during the first minute of actin flows. N=3, n=3. (**G**) Averaged F-actin flow velocity along the AV axis of control (blue, N=3, n=3) and CAMypt overexpressing (red, N=4, n=4) oocytes. (**G'**) Bar chart of the data in (G). (**H**) Ooplasm (N=3, n=7) and F-actin (N=4, n=4) flow velocities in CAMypt overexpressing oocytes during the peak of the first bulk actin polymerization wave. F-actin flow speed data from (G). Error bars, SEM. Mann-Whitney test, ns: not significant, ***** P <0.0001.*

Figure 6. Generation and directionality of F-actin flows within the oocyte.
(**A**) Theoretical prediction of fluid accumulation along the AV axis of the oocyte in the presence of a pre-patterned actin gradient. (**B**) Theoretical (left) and experimental (right) kymographs of F-actin intensity along the AV axis of the oocyte during phase segregation. Numerical simulations were performed with a pre-patterned gradient of actin as in (A) and noisy initial conditions. (**C**) Theoretical prediction of fluid accumulation along the animal-vegetal (AV) oocyte axis in the absence of a pre-patterned F-actin gradient. (**D**) Normalized bulk actin intensity along the AV oocyte axis prior to bulk actin polymerization wave formation for control (DMSO, blue, N=3 experiments, n=3 oocytes) and Cytochalasin B-treated (Cyto B, green, N=3, n=5) oocytes (top plot), and for control (DMSO, blue, N=4, n=6) and Jasplakinolide-treated (Jasp, red, N=5, n=12) oocytes (bottom plot). (**E**) Images (first two columns from the left) of oocytes expressing Utr-GFP to mark F-actin treated with Cyto B (upper row) and Jasp (lower row) prior and during wave formation. Third column from the left: averaged velocity vector field of bulk actin flows during the first actin wave. + velocities, animalward flows; - negative velocities, vegetalward flows. Fourth column from the left: brightfield (BF) images of oocytes treated with Cyto B (upper panel) and Jasp (lower panel) after the second cleavage. (**F**) Theoretical (left, taken from the numerical simulations of (C)) and experimental (measured from E; treated with Cyto B (middle) or Jasp (right)) kymographs of bulk actin intensity along the AV axis of oocytes as a function of time. Hot-to-cold color coding corresponds to high-to-low actin intensity. Error bars, SEM. Mann-Whitney test, ns: not significant, ** P =0.0421, ** P =0.0054.*

Figure 7. Actin comet formation in ooplasm-yolk granules segregation.
(**A**) YG velocity vector field taken from 2D flow simulations with a zero-stress bastodisc-YGs interface (BYI). The box corresponds to zoomed-in view of YGs velocity vector field at BYI. Color code ranges from high + (red) to high - (blue) velocities. (**B**) Images of oocytes expressing Rac1-NGreen to mark ooplasm and YGs. Dashed white lines indicate BYI. Green dashed line is used for the kymograph in Figure S7B. **(C)** Averaged central BYI displacement (cyan, left axis) and ooplasm flow velocity (magenta, right axis) from 30 to 70 mpf. N=3 experiment, n=5 oocytes. Ooplasm flow velocity data are taken from Figure 1G. The green and golden boxes indicate the straightening and protruding phases when the central BYI changes its shape. (**D**) Images of oocytes expressing Utr-GFP to mark F-actin (red) and exposed to NileRed to mark YGs (green). White and blue boxes indicate the ROIs used for measuring actin intensity in the ooplasm or on the YGs surface

in D', respectively. Yellow ROI indicates the area used for zoomed-in images in (D''). (**D'**) Ratio of actin intensities on YGs surface (blue box in D) relative to ooplasm (yellow box in D) during bulk actin polymerization wave. N=3, n=3. (**D''**) Zoomed-in view of YGs and bulk actin at the ROI indicated in (D). Arrowheads demarcate the formation of actin comets on the ooplasm facing side of YGs. (**E**) Averaged displacement of YGs at the BYI during bulk actin polymerization wave. Period of wave propagation is marked in green. N=2, n=2. (**F**) Kymograph of YGs (green) and F-actin (red) displacement along the AV axis as a function of time. Kymograph was taken at the position within the oocyte marked by white dashed line in (C, left panel). Arrowheads demarcate actin on YGs surface. (**G**) Images of F-actin in oocytes. Yellow arrowheads indicate comet formation events around several YGs at the BYI.(**H**) Images of F-actin (red) and YGs (green and segmented in cyan) in oocytes . **(I)** Measured (left, averaged from Particle Image Velocimetry (PIV) analysis of YGs over the first 5 min of the first protruding phase, N=1, n=3) and simulated (right, in the absence of stress at BYI) YGs velocity vector fields during the protruding phase. Color code ranges from high + (red) to high - (blue) velocities. **(I')** Measured (left, averaged from PIV analysis of YGs over the first 5 min of the second straightening phase, N=1, n=3) and simulated (right, in the presence of stress at BYI) YGs velocity vector fields during the straightening phase. The box corresponds to zoomed-in view of YGs velocities at BYI. **(J)** Images of F-actin in WT (top row) and *Dchs* mutant (bottom row) oocytes during the first two actin polymerization waves. Arrowheads indicate actin comet formation on YGs surface at BYI. **(K)** Ratio of actin intensities on YGs surface relative to ooplasm during bulk actin polymerization wave for WT (cyan, N=3, n=6, same data as in D') and *Dchs* mutant oocytes (magenta, N=3 , n= 8). **(L)** Amplitudes of actin oscillations during the first three actin polymerization waves for WT (cyan, N=3, n=5) and *Dchs* mutant oocytes (magenta, N=3 , n=5). Error bars, SEM. Mann-Whitney tests, ns: not significant, ***** P <0.001.*

SUPPLEMENTARY FIGURE LEGENDS

Figure S1: Spatiotemporal correlation between ooplasm flows and changes in cortical actomyosin. Related to Figure 2.

(**A**) Fluorescence images of oocytes expressing Utr-GFP to mark F-actin. Scale bar, 50 μm. (**B**) Averaged cortical actin intensity (red, left y-axis, N=3 experiments, n=3 oocytes) and beads speed as readout of ooplasm flows (blue, N=3 experiments, n=7 oocytes, taken from Figure 1C.) during the first 100 mpf. Error bars, SEM. (**C**) Averaged length of the cortex at the animal pole (AP) of the oocyte as readout of animal pole deformation during the first ooplasm flow cycle. Error bars, SEM. N=3 experiments, n=6 oocytes. (**D**) Fluorescence images of UV laser cuts of the cortex at the animal pole of oocytes expressing Utr-GFP to mark F-actin. Left and right panels shows cortex before and after the cut, respectively. Scale bar, 15 μm. (**D'**) Particle Image Velocimetry (PIV) analysis of cortical flows surrounding the cut (outlined by golden box in middle panel) following the cut. Scale bar, 5 μm. (**E**) Recoil velocity of the actin cortex as a function of frames post cut (each frame is 200 ms) at 3 different stages of the oocyte: 15-30 mpf (red, before the first cycle of ooplasm flow), 30-40 mpf (green, during the first cycle of ooplasm flow), and 40-50 mpf (blue, after the first cycle of ooplasm flow). Error bars, SEM. (**F**) Initial recoil velocities for the different conditions described in (E) calculated shown as kernel densities (top) and box whisker plots (bottom). Color codes are as described in (E). *** P =0.0019,* ns: not significant, Mann-Whitney test. (**G**) Schematic illustrating how changes in cortical tension at the animal pole of the oocyte could trigger ooplasm flows.

Figure S2: Requirement of the actomyosin cytoskeleton for ooplasm-yolk granules segregation. Related to Figure 2.

(**A**) Fluorescence/bright-field images of oocytes exposed to DMSO (control), Nocodazole (50 µg/ml) or Cytochalasin B (Cyto B, 100 µg/ml) or injected with CAMypt mRNA (85 pg/embryo) at 100 mpf. Oocytes were also injected with Dextran-Alexa Fluor 647 (cyan) to label the ooplasm, polystyrene beads (red, 2 μm) to track ooplasm flows, and Ras-eGFP (130 pg/embryo) for controlling the CAMypt overexpression (OE) experiments. Scale bars, 100 μm. (**B**) Averaged speed of injected beads as readout of ooplasm flows during the first 100 mpf. Upper plot: DMSO, blue with N=3 experiments, n=3 oocytes; Cytochalasin B (Cyto B), red with N=3 experiments, n=3 oocytes; Nocodazole, green with N=4 experiments, n=4 oocytes. Lower plot: Ras-eGFP, blue with N=3 experiments, n=3 oocytes; CAMypt, red with N=2 experiments, n=2 oocytes. (**C**) Normalized and averaged distance of beads to the animal pole of the oocyte during the first 100 mpf. Color coding and N/n as in (B). 0 and 1 on y-axis correspond to animal and vegetal poles, respectively. (**D**) Averaged speed of marginal YGs marked by 1% NileRed during the first 100 mpf. Color coding and N/n as in (B). Error bars, SEM.

Figure S3: Speed analysis of bulk F-actin polymerization wave. Related to Figure 2.

(**A**) Fluorescence image of an oocyte expressing Utr-GFP to mark F-actin. White semi-circles indicate the ROIs used for measuring the actin intensity in different distances from the center of the wave. Scale bar, 100 μm. (**B**) Normalized and averaged actin intensity for different distances from

the wave centre using the circular ROIs as indicated in (A) for the duration of the first cycle (0-50 mpf). The dashed black arrow marks the maxima of each curve, indicating polymerization wave propagation. (**C**) Kymograph of actin movement along the animal-vegetal (AV) axis of the oocyte as a function of time. White dashed lines trace the bulk actin polymerization waves during the first 3 cleavages. Scale bars, 25 μm (y-axis) and 10 min (x-axis). (**D**) Speed of the actin polymerization wave. Box and whiskers, min to max. N=4 experiments, n=4 oocytes.

Figure S4: Analysis of ooplasm and yolk granules flows in oocytes with altered Cdk1 dynamics. Related to Figure 3.

(**A**) Normalized and averaged ooplasmic actin intensity for the duration of one cell cycle (0-50 mpf). I1, interphase of the 1st cycle, M1, metaphase of the 1st cycle and A1, anaphase of the 1st cycle . Error bars, SEM. N=1 experiment, n=1 oocyte measured on 5 different stacks. (**B**) Averaged ooplasm flows in control (blue, N=3 experiments, n=7 oocytes), Wee1 inhibitor treated (red, N=1 experiment, n=3 oocytes), Chk1 over expressing (Chk1-OE, green, N=1 experiment, n=3 oocytes) and Cdk1 inhibitor treated (black, N=2 experiments, n=4 oocytes) oocytes during the first 100 mpf. Error bars, SEM. (**C**) Averaged speed of marginal (left plot) and central (right plot) YGs in control (blue, N=1 experiment, n=2 oocytes, measured on 5 different stacks with z=10 slices), Wee1 inhibitor treated (red, N=1 experiment, n=2 oocytes, z=6 slices), Chk1 overexpressing (Chk1-OE, green, N=1 experiment, n=2 oocytes, z=10 slices) and Cdk1 inhibitor treated (black, N=2 experiments, n=6 oocytes, z=6 slices) oocytes during the first 100 mpf. Error bars, SEM.

Figure S5: Rheological analysis of the ooplasm, F-actin and yolk granules. Related to Figures 4 and 5.

(**A**) Normalized and averaged intensity of the bulk actin within the ooplasm along the animal-vegetal (AV) axis of the oocyte prior to actin wave formation in unconfined (WT, data taken from Figure 4A') and spatially confined (N=3 experiments, n=8 oocytes) oocytes. Error bars, SEM. Note that the gradient of bulk actin along the AV axis of the oocyte is preserved even when the oocyte is flattened (spatially confined), suggesting that the observed actin gradient is not due to signal quenching by YGs in the oocyte center. (**B**) Kymograph of actin intensity along the animal-vegetal (AV) axis of the oocyte as a function of time. Yellow arrowheads trace F-actin bundles flowing towards the animal pole (AP). Scale bars, 25 μm (y-axis) and 2 min (x-axis). (**C**) Fluorescence images of F-actin (magenta, left panel), Myosin-2 (cyan, middle panel) and merged F-actin & Myosin-2 (right panel), illustrating their colocalization. Scale bars, 50 μm . (**D**) Kymograph of F-actin intensity along the line perpendicular to the laser ablation site and prior to actin polymerization wave. Hot-to-cold color coding corresponds to high-to-low actin intensity. White arrowheads trace the recoil of the bulk actin after ablation. Scale bars, 5 μm (y-axis) and 5 s (x-axis). (**E**) Kymograph of F-actin intensity changes perpendicular to the laser ablation site after ablation during the bulk actin polymerization wave. Hot-to-cold color coding corresponds to high-to-low actin intensity. White arrowheads trace the recoil of the bulk actin network after ablation. Scale bars as in B. (**E'**) Initial recoil velocities measured for laser cuts performed prior (red) and during (blue) bulk actin polymerization wave formation, obtained by fitting a linear curve to the first four post-cut data points in (Figure 5F) and measuring the slope. Error bars, SEM. ** *P*

=0.0037, Mann-Whitney test. (**F**) Fluorescence images of oocytes injected with 70 KDa Dextran-Alexa Fluor 647 to label the ooplasm for Fluorescence Recovery After Photobleaching (FRAP) experiments. Golden box outlines the bleached area (41.5 * 8.3 μm^2). Scale bar, 25 μm . (**F'**) Normalized and averaged Dextran intensity of the bleached area over time. N=4 experiment, n=36 oocytes. Calculated diffusion coefficient and corresponding ooplasmic viscosity (from Stokes-Einstein relationship; for details see Methods): 1.9 µm^2/s and 20 mPa.s (**G**) Bright-field images of oocytes before (left column) and at the end (right column) of pipette aspiration to measure ooplasm viscosity within the blastodisc dominated by F-actin. Scale bar, 100 μm . Black arrowhead indicates how far the ooplasm has flown in the pipette. (**G'**) Box and whiskers plot of measured blastodisc viscosities from pipette aspiration assay. "+" sign indicates the mean. N=3 experiments, n=23 oocytes. (**G''**) Box and whiskers plot of measured blastodisc viscosities from pipette aspiration assay in DMSO (Cyan, N=3 experiments, n=15 oocytes) and Cytochalasin B (Cyto B, magenta, N=4 experiments, n=16 oocytes) treated oocytes. This result indicates that the bulk actin accounts largely for the measured blastodisc viscosity in control oocytes. "+" signs indicate the mean. **** P <0.001, Mann-Whitney test. (**H**) Box and whiskers plot of YGs mesh size obtained by measuring the shortest axis of fluid pockets between YGs. "+" sign indicates the mean. N=3 experiments, n=3 oocytes. (**I**) Bright-field images of oocytes before (left column) and at the end (right column) of pipette aspiration to measure YGs viscosity. Scale bar, 100 μm . Black arrowhead indicates how far yolk has flown in the pipette. (**I'**) Averaged yolk tongue displacement (deformation) during the aspiration and relaxation time points. Black arrowhead indicates the end of aspiration. N=3 experiments, n=21 oocytes. Error bars, SEM. (**I''**) Box and whiskers plot of measured yolk viscosities from pipette aspiration assay. "+" sign indicates the mean. N=3 experiments, n=26 oocytes. (**J**) Normalized ooplasm flow velocities away from the peak of the flows and along the animal-vegetal (AV) axis of the oocyte (averaged for the duration of the first cell cycle). Solid line, exponential fit with the length scale of $\sim 160 \mu m$. Error bars, SD. N=1 experiment, n=3 oocytes.

Figure S6: Generation and directionality of F-actin flows within the oocyte. Related to Figure 6.

(**A**) Theoretical fraction of ooplasm transported at the animal pole (after three numerical oscillations) as a function of the strength of the pre-patterned F-actin gradient in the oocyte (for details see Methods). Each point is the result of averaging over 50 simulations with random initial conditions. Without gradient, ooplasm accumulates dominantly in the center, while for strong gradients, the accumulation is robustly localized at the animal pole . (**B**) Fluorescence images of oocytes expressing Utr-GFP to mark F-actin for control (left), Cytochalasin B (middle) and Jasplakinolide (right) treated cases. Yellow ROIs indicate the area used for acquiring the F-actin kymographs in Figures 6B and 6F. Scale bars, 100 μm . (**C**) Theoretical prediction of rescaled F-actin speed along the AV oocyte axis before and during the first three actin wave cycles and in the presence of a pre-patterned F-actin gradient. (**C'**) Kymograph of actin taken from flow simulations in Figure 6A (i.e. with pre-patterned gradient of actin and without noise in initial conditions). Hot-to-cold color coding corresponds to high-to-low actin intensity. Scale bars, 100 μm (y-axis) and 10 min (x-axis). (**D**) Theoretical prediction of rescaled F-actin velocity along the AV oocyte axis

before and during the first three actin wave cycles and in the absence of a pre-patterned F-actin gradient. (**D'**) Kymograph of actin taken from flow simulations in Figure 6C (i.e. without pre-patterned gradient of actin and without noise in initial conditions). Hot-to-cold color coding corresponds to high-to-low actin intensity. Scale bars, 100 μm (y-axis) and 10 min (x-axis). (**E**) Ratio of oocytes with complete segregation (1 if ooplasm accumulating at the animal pole and 0 if ooplasm accumulating at the center) for control (DMSO, blue, N=7 experiments, n= 9 oocytes), Cytochalasin B-treated (Cyto B, green, N=4 experiments, n=5 oocytes) and Jasplakinolide-treated (Jasp, red, N=6 experiments, n= 12 oocytes) oocytes. Error bars, SEM. **** P =0.0005,** P =0.0046*, Mann-Whitney test.

Figure S7: Actin comet formation in ooplasm-yolk granules segregation. Related to Figure 7. (**A**) Normalized ooplasm accumulation along the lateral (Lat) axis of the oocyte. N=2 experiments, n=6 oocytes. Error bars, SEM. 0 and 300 μm correspond to the center and margin of the oocyte, respectively. (**B**) Shape of the blastodisc-YGs interface (BYI) of the oocyte at 30 mpf (red) and 35 mpf (blue). N=3 experiments, n=3 oocytes. Error bars, SEM. (**C**) Kymograph of ooplasm and YGs marked by Rac1-NeonGreen taken along the green dashed line in Figure 7B. White dashed line outlines BYI during the first three cell cycles. Scale bars, 25 μm (y-axis) and 10 min (x-axis). (**D**)Fluorescence image of oocytes expressing Utr-GFP to mark F-actin (red) and exposed to NileRed to mark YGs (green) . Same oocyte as in (Figure 7D). Yellow ROI indicates the area used for zoomed-in images in (D'). Scale bar, 100 μm. (**D'**) Zoomed-in view of YGs and bulk actin at the ROI indicated in (D). Arrowheads indicate the formation of actin comets on the ooplasm facing side of YGs. Scale bar, 25 μm. (**E**) Fluorescence image of oocytes expressing Utr-GFP exposed to DMSO (control), CK666 (Arp2/3 inhibitor, 300 μM) or SMIFH2 (Formin inhibitor, 300 μM). Yellow and white boxes indicate the ROIs used for measuring actin on YGs surfaces in (E'). Scale bar, 25 μm. (**E'**) Differential actin intensities during actin bulk actin polymerization wave propagation (white boxes) normalized to actin prior to wave formation (yellow boxes) on YGs surface for control (DMSO, blue, N=3 experiments, n=5 oocytes), CK666-treated (green, N=3 experiments, n=6 oocytes) and SMIFH2-treated (red, N=3 experiments, n=6 oocytes) oocytes. Error bars, SEM. ***** P <0.0001,* ns: not significant, Mann-Whitney test. **(F)** Fluorescence images of oocytes expressing Utr-GFP to mark F-actin with additional YGs transplanted from a donor oocyte into its blastodisc prior to bulk actin polymerization wave formation at 24, 30 and 41 mpf. Scale bar, 100 μm. (**F'**) Kymograph of actin intensity marked by Utr-GFP expression along the yellow dashed line in (F) as a function of time. Hot-to-cold color coding corresponds to high-to-low actin intensity. Scale bars, 50 μm (y-axis) and 2 min (x-axis). **(G)** Schematic illustrating the vegetalward movement of the bulk actin polymerization wave (green), flows of bulk actin towards the animal pole (red), and actin comet formation at BYI, pushing YGs towards the vegetal pole. Green dashed line outlines the leading front of the bulk actin polymerization wave. **(H)** Fluorescence images of *Dchs* mutant oocytes expressing Utr-GFP to mark F-actin, with several of the "escaping" YGs being segmented. Scale, 100 μm.

SUPPLEMENTAL INFORMATION

STAR METHODS

CONTACT FOR REAGENT AND RESOURCE SHARING

Further information and requests for resources, reagents, data, and code should be addressed to the Lead Contact, Carl-Philipp Heisenberg (heisenberg@ist.ac.at).

EXPERIMENTAL MODEL AND SUBJECT DETAILS

Fish maintenance and embryo/oocyte collection were carried out as described (Westerfield 2007). Oocytes were raised in E3 or 1x Danieu's medium buffer and kept at 25-31°C for further experimentation. Fish were bred in the zebrafish facility at IST Austria according to local regulations, and all procedures were approved by the Ethic Committee of IST Austria regulating animal care and usage.

METHOD DETAILS

Transgenic and mutant zebrafish lines

For live imaging of F-actin, oocytes from *Tg(actb1:Utr-GFP)* and *Tg(actb1:Utr-mCherry)* were used (Krens et al. 2017; Behrndt et al. 2012). For imaging of non-muscle Myosin regulatory light chain and microtubules, oocytes from *Tg(actb1:myl12.1-GFP)* and *Tg(XlEef1a1:dclk2-GFP)* were used, respectively (York et al. 2012; Maître et al. 2012). For simultaneous visualization of ooplasm and yolk granules, *Tg(actb1:mNeonGreen-Rac1a)* zebrafish line ubiquitously expressing NeonGreen-tagged Rac1 was generated using the Tol2/Gateway technology (Kwan et al. 2007; Villefranc, Amigo, and Lawson 2007). Briefly, the coding sequence of *rac1a* (NCBI reference sequence: NM_199771.1) was amplified using gene specific primers with additional Gateway recombination arms (5'- GGGGACAGCTTTCTTGTACAAAGTGGCTATGCAGGCCATAAAGTGTG-3' and 5'-GGGGACAACTTTGTATAATAAAGTTGCTCACAGAAGGAGACATCTTCTC-3') from cDNA library of sphere stage wild type Tübingen embryos. The PCR product was recombined with *pDONR P2r-P3* (Lawson#211) and the resulting entry clone after sequence verification was recombined with *pDestTol2pA2* (Chien#394), *p5E β-actin* promoter (Chien#229) and *pME NeonGreen* (Shaner et al. 2013) with *mNeonGreen* licensed by Allelebiotech to create *pTol2-β-actin::NeonGreen-Rac1a*. The *pTol2* vector was co-injected with mRNA encoding the transposase (Invitrogen) into 1 cell-stage wild type TL embryos. Individual positive carriers were selected and out-crossed with wild type TL fish for stable single-copy genetic integration. $dchs1b^{fh275}$ (*Dchs*) mutant oocytes were kindly provided by L. Solnica-Krezel (Li-Villarreal et al. 2016). The oocytes were then raised and their offsprings were used for experiments. For analysing F-actin dynamics in *Dchs* mutant oocytes, we generated ($dchs1b^{fh275}$, *Tg(actb1:Utr-GFP)*) fish by crossing the two lines.

mRNA injections

The following expression constructs were used:
CAMypt (Smutny et al. 2017; Weiser, Row, and Kimelman 2009), *ras-eGFP* (Morita et al. 2017) and *chk1* (see below). mRNA was Synthesized using the SP6 mMessage mMachine Kit (Ambion). Injections into oocytes were performed at 5 to 10 mpf as described (Westerfield 2007) using glass capillary needles (30-0020, Harvard Apparatus, MA, USA) ,which were pulled by a needle puller (P-97, Sutter Instrument) and attached to a microinjector system (PV820, World Precision Instruments). 85-150 pg of *CAMypt*, 130 pg of *ras-GFP* and 250 pg *chk1* mRNA were injected into 1-cell stage embryos. To synthesize *chk1* mRNA, Gateway technology (Invitrogen) was used to create *pCSDest2* vector containing the sequence of *chk1*. The coding sequence of *chk1* (NCBI reference sequence: NM_200193) was amplified using gene specific primers with additional Gateway arms (5'-GGGGACAAGTTTGTACAAAAAAGCAGGCTTAATGGCTGTGCCTTTTGTTAAAG-3' and 5'- GGGGACCACTTTGTACAAGAAAGCTGGGTATCAAATCAATGGCAAAACC-3') from cDNA library of sphere stage wild type Thübingen embryos. The PCR product was recombined with *pDONR221* (Lawson#208) and the resulting entry clone after sequence verification was recombined with *pCSDest2* (Lawson #444) and *p3E-polyA* (Chien#302) to create the vector used for mRNA synthesis (mMessage mMachine SP6 transcription kit, Thermofisher).

Sample preparation for live imaging

Oocytes were mounted in 0.3% low melting point (LMP) agarose (Invitrogen) in E3 medium inside a glass bottom petri dish (MateTek) for live imaging. For drug treatment experiments, Cytochalasin B (Sigma, 100 $\mu g/ml$), Jasplakinolide (Tocris Bioscience, 50 μM), PD0166285 (abcam, 200 μM), Dinaciclib (Selleckchem, 200 μM), Nocodazole (Sigma ,50 $\mu g/ml$), SMIFH2 (Sigma, 300 μM), CK666 (Sigma, 300 μM) and DMSO (Sigma) were used. For labeling the yolk granules in Figure S2, oocytes were treated with NileRed (ThermoFisher, 10 μM). Oocytes were initially kept in E3 solution containing the drug (and/or NileRed) for 10 min, and then transferred to the drug containing 0.3 % LMP agarose for the duration of the imaging. To label the ooplasm, 1 nl of 2 mg/ml of 10 KDa Dextran Alexa Fluor (10,000, Invitrogen) was injected to the center of the oocyte. FRAP experiments were performed on oocytes injected with 70 KDa Dextran-Alexa 647 (70,000, ThermoFisher).

Whole oocyte confocal imaging

For whole oocyte confocal imaging, oocytes were imaged using an inverted Leica SP5 confocal microscope equipped with Leica 20x 0.7 NA or 10x 0.4 NA objectives. The temperature during imaging was kept constant at 30 ± 1 C° using a stage heating device (Life Imaging services). Typically, imaging stacks ranging between 100 and 200 μm beneath the oocyte membrane were recorded.

Confocal imaging of confined and cortex-free oocytes

PDMS based cubic boxes (700 x 700 x 500 μm^3) were manufactured in order to spatially confine the oocytes. Newly fertilised oocytes were positioned in the cubic boxes in E3 medium. The boxes were closed with a coverslip to spatially confine the oocytes. For generating 'cortex-free' oocytes, the glass coverslip was pressed slightly harder on the oocytes within the box, thereby breaking their plasma membrane and cortex. Confocal Zeiss LSM 700 Upright or Zeiss LSM 880 Upright microscopes were used for imaging of the confined/cortex-free oocytes. The temperature during imaging was kept constant at 30 ± 1 C° using a temperature chamber (Life Imaging services).

Beads speed and displacements measurements

To analyze ooplasm flows, 2 μM polystyrene beads (ThermoFisher) were diluted 1:5 in 10% glycerol in H2O. 1nl of the diluted solution was injected to the oocytes centre at 5-10 mpf. Oocytes were then mounted and imaged as described. The injected beads were followed over time using Imaris 9.1.2, and the acquired tracks were then post-processed in Matlab R2017b to obtain their velocity. Only beads, which were initially located in the oocyte centre, were used for analysis. To determining bead distance from animal pole (Figure S2C), the distance between the averaged position of the beads to the initial animal pole position was measured and then normalized to the initial length of the animal-vegetal oocyte axis.

F-actin intensity measurements

To measure F-actin intensity within the cortex or ooplasm in *Tg(actb1:Utr-GFP)* oocytes, rectangular shaped ROIs were defined for the corresponding regions, and the averaged intensities over time were obtained using Fiji. For measuring the speed of the bulk actin polymerization wave within the ooplasm, first actin distribution within the wave was determined by measuring F-actin intensity in ROIs that were defined by semi-circles with radii varying from 10 to 145 μm and centered at the central point of the wave. The speed of the polymerization wave was then measured by tracking the peak of the acquired actin intensity profiles. For obtaining the F-actin intensity profile along the entire animal-vegetal axis of the oocyte, first F-actin fluorescence was segmented using Ilastik software (Sommer et al. 2011). The segmented pockets were then used as ROIs for measuring F-actin intensity using Analyze Particles command in Fiji. Actin measurements were eventually transferred to Matlab to average the intensity values according to their corresponding ROI area and sort them along the animal-vegetal axis of the oocyte.

Animal pole cortical deformation measurements

To measure animal pole cortical deformation, *Tg(actb1:Utr-GFP)* oocytes were imaged using a Leica 20x 0.7 NA objective. Animal pole cortex was then segmented using Ilastik software, and the segmented images were post-processed by a custom-designed Matlab script, with the help of which the 2D segmented cortical area was converted to a line used for measuring cortical length.

Yolk granules and ooplasm segmentation and velocity measurements

To simultaneously analyze ooplasm flows and yolk granules movements, fluorescence images of oocytes expressing Rac1-NGreen were segmented using Ilastik software. The segmented images of the ooplasm or yolk granules were then used for PIV analysis using PIVlab (Thielicke and Stamhuis

2014), and post-processed by a custom-designed Matlab script. Central yolk granules velocities were averaged for the 300-400 µm of the middle of the egg and marginal granules velocities were averaged over 50-75 µm (on each side) close to the cortex.

Mini-embryo preparation

Using an eyelash knife, a newly-fertilized oocyte was cut in half at its equator perpendicular to its animal-vegetal axis. The resulting two half embryos (animal-half and vegetal-half) were left for a few minutes to heal their wounding sites and round up in culture medium (E3) and then used for further experimentation.

Cortical laser ablation

Cortical tension was measured by conducting cortical laser ablations on a UV laser ablation setup equipped with a Zeiss 63x 1.2 NA water immersion lens using *Tg(actb1:Utr-GFP)* oocytes (Behrndt et al. 2012). Cortical laser ablations were performed at various time points of the first cell cycle by applying 25 ultraviolet pulses at 1000 Hz to 40 equidistant sites along a 20 µm-long line using exposure times of 150 ms and 0.2 s frame rates. The laser ablation itself lasted 1.2 s during which no images were acquired. All ablation experiments were performed at room temperature. Cortical recoil velocity after cortical laser ablation was quantified using PIVlab. The temporal recoil velocities were measured for consecutive post-cut frames (up until 20 frames) by averaging the component of the calculated velocity in the perpendicular direction to the cut an area of $20\ x\ 20\mu m^2$ surrounding the cut site.

Ooplasm laser ablation

Ooplasm laser ablations were performed with the same settings as cortical laser ablations, with the difference that the ooplasmic cuts were performed between 20 to 30 µm beneath the cortex. To analyse the ooplasm recoil velocity after laser ablation, a kymograph was acquired from a line scan perpendicular to the cut position to represent pre- and post-cut states of the cut area as (Smutny et al. 2015). The kymograph was segmented using Ilastik software , and the segmented image was analysed by a custom-designed Matlab script to measure the recoil distance over time. The initial recoil velocity was measured from the slope of the linear fit to the first 4 post-cut recoil distances.

High-resolution confocal imaging of F-actin flows within the ooplasm

For high-resolution confocal imaging of F-actin within the ooplasm, *Tg(actb1:Utr-GFP)* oocytes were used. Imaging was performed on a spinning disk setup (Andor Revolution Imaging System; Yokogawa CSU-X1) equipped with a Zeiss 40x 1.2 NA water immersion lens (Behrndt et al. 2012). To capture the dynamics of actomyosin flows within the bulk of the ooplasm, small z-stacks (19; 1 µm step size; 300 ms exposure time) were selected to achieve short time intervals of 9 s. Only superficial stacks just beneath the cortex were analyzed , as signal intensity sharply dropped deeper in the oocyte. Flow velocities were quantified using PIVlab on the maximum intensity projections of the z-stacks excluding the cell cortex. Velocity kymographs were obtained by averaging the animalward velocities over the lateral axis of the oocyte. Time-lapses typically lasted for 1 h during which the sample was kept at constant temperature of 30±1C° using a stage heater.

Pipette aspiration experiments

To determine the viscosity of F-actin, the viscosity of the ooplasm within the blastodisc was measured using pipette aspiration, considering that macroscopic rheological properties of the ooplasm are most likely dominated by F-actin. In addition, pipette aspiration was used on yolk granules to determine whether they can be approximated as simple newtonian fluid with a given viscosity. Pipette aspiration experiments were performed on oocytes mounted on 3% methylcellulose in 1x Danieu's using an inverted Leica SP5 confocal microscope equipped with the micropipette aspiration system (K. Guevorkian and Maître 2017; Karine Guevorkian et al. 2010). For aspirating ooplasm or yolk granules, fire-polished and with heat inactivated FBS passivated micropipettes with an inner diameter of 60 µm, 30° bent, and with a spiked end (Biomedical Instruments) were inserted into the blastodisc (ooplasm) or center of the oocyte (yolk granules). Upon insertion, an aspiration pressure of 30 Pa was applied using a Microfluidic Flow Control System Pump (Fluigent, Fluiwell; negative pressure range, 7-750 Pa; pressure accuracy, 7 Pa; change rate, 200 Pa.s-1) and Dikeria micromanipulation software. Pressure was applied while the blastodisc ooplasm or yolk entered into the pipette with a constant velocity for about 50 s, after which the pressure was released. Brightfield images were taken every 1.5 s using a Leica 10x 0.4 NA objective. Experiments were performed at room temperature. Viscosity calculations were performed as described (K. Guevorkian and Maître 2017). In short, the deformations during aspiration and relaxation were plotted, and the slope of the aspiration curve at the point of constant flow was obtained from the corresponding kymographs. The aspiration slope depends on the viscosity with $L_{asp} = \frac{R_p(P-P_c)}{3\pi\eta}$, where R_p is radius of the pipette, P the applied pressure and P_c the critical pressure. When the pressure is released, the the slope of the ooplasm retraction velocity depends on the viscosity with $L_{ret} = \frac{R_p(P_c)}{3\pi\eta}$. From the aspiration and retraction rates, viscosity can then be calculated as $\eta = \frac{R_p(P)}{3\pi(L_{asp}+L_{ret})}$.

Yolk granule to blastodisc transplantations

Yolk granules from the centre of a donor oocyte were transplanted into the blastodisc of a host oocyte at the same stage. For transplantation, a beveled fire-polished transplantation needle with a 80 µm inner diameter (Biomedical Instruments) connected to an air-filled syringe system was used.

Fluorescence Recovery After Photobleaching (FRAP)

FRAP experiments were performed on oocytes injected with 70 KDa Dextran-Alexa 647. Images were taken on a confocal Zeiss LSM 880 Upright microscope equipped with a 20x NA 1.0 Water immersion lens. The bleached area was set as a rectangle of 41.5 x 8.3 μm^2 size. The time course of fluorescence recovery was tracked by measuring the average intensity of the bleached area over time. The normalized intensity measurements were fitted as described (Ellenberg et al. 1997) based on the following relationship: $I = a_0 + a_1(1 - \sqrt{\frac{w^2}{w^2+4\pi Dt}})$, where w is the width of the bleached rectangle. Ooplasm viscosity was determined by implementing the available hydrodynamic radius of 70 KDa Dextran (about 6nm (Armstrong et al., 2004)) and the measured diffusion coefficient into the Einstein equation $\eta = \frac{K_b T}{(6\pi DR)}$ with K_b the Boltzmann constant, T the temperature, D the diffusion coefficient and R the hydrodynamic radius.

Yolk granule mesh size

Yolk granule mesh size was approximated by measuring the shortest axis of several ooplasm pockets within oocytes.

QUANTIFICATION AND STATISTICAL ANALYSIS

Statistical analysis was performed using Prism 8 (GraphPad Software). Data are represented as mean ± SEM (stated otherwise) and analyzed with the Mann-Whitney test or t-test. A p value < 0.05 was considered statistically significant.

SUPPLEMENTARY MOVIE LEGENDS

Movie 1:
Related to Figure 1. Time-lapse bright-field (left) and fluorescence (right) movie (45 s interval) of an exemplary zebrafish oocyte injected with Dextran-Alexa Flour 647 to label the ooplasm during the first 100 min post fertilization (mpf). Scale bar: 100 μm. Time: 29 to 100 mpf.

Movie 2:
Related to Figure 1. Time-lapse fluorescence/bright-field movie (25 s interval) of an exemplary oocyte injected with Dextran-Alexa Flour 647 (Magenta) and polystyrene beads (red, 2 μm) to mark ooplasm flows. Scale bar: 100 μm. Time: 30.75 to 100 mpf.

Movie 3:
Related to Figure 1. Time-lapse fluorescence movie (67 s interval) of an exemplary oocyte expressing Rac1-NeonGreen to mark ooplasm and yolk granules. Scale bar: 100 μm. Time: 25.5 to 100 mpf.

Movie 4:
Related to Figure S1. Time-lapse fluorescence movie (52 s interval) of an exemplary oocyte expressing Utr-GFP to mark F-actin during the first 100 mpf. Sum intensity projection. Hot-to-cold color coding corresponds to high-to-low actin intensity. Scale bar, 100 μm.

Movie 5:
Related to Figure S2. Time-lapse fluorescence/bright-field movie (top 42 s and bottom 47 s interval) of exemplary oocytes injected with Dextran-Alexa Flour 647 (cyan) and polystyrene beads (red, 2 μm) to mark ooplasm flows and top: treated with DMSO (left), Nocodazole (middle, 50 $\mu g/ml$) or Cytochalasin B (right, 100 $\mu g/ml$), bottom: injected with Ras-eGFP (left, 130 pg) or CAMypt (right, 85 pg). Scale, 100 μm. Time: 25 to 100 mpf.

Movie 6:
Related to Figure 2. Time-lapse fluorescence/bright-field movie (17 s interval) of exemplary oocytes injected with polystyrene beads (red, 2 μm) to mark ooplasm flows and left: confined in squared-shaped boxes (700 x 700 x 500 μm^3) and right: stabbed to break the plasma membrane and confined in squared-shaped boxes (700 x 700 x 500 μm^3). Scale bar: 100 μm. Time: 24 to 100 mpf.

Movie 7:
Related to Figure 2. Time-lapse fluorescence movie (60 s interval) of an exemplary oocyte expressing Utr-GFP to mark F-actin, stabbed to break the plasma membrane and confined in squared-shaped boxes (700 x 700 x 500 μm^3). Scale bar: 100 μm. Hot-to-cold color coding corresponds to high-to-low actin intensity. Time: 28 to 100 mpf.

Movie 8:
Related to Figure 2. Time-lapse fluorescence movie (51 s interval) of an exemplary oocyte expressing Utr-GFP to mark F-actin. Scale bar: 100 μm. Hot-to-cold color coding corresponds to high-to-low actin intensity. Time: 27 to 100 mpf.

Movie 9:
Related to Figure 2. Time-lapse fluorescence movie (1 s interval) of an exemplary oocyte expressing Utr-GFP to mark F-actin. Scale bar: 100 μm. Hot-to-cold color coding corresponds to high-to-low actin intensity. Time: 29 to 100 mpf.

Movie 10:
Related to Figure 3. Time-lapse fluorescence movie (35 s interval) of an exemplary oocyte expressing DCLK-GFP (cyan) and Utr-mCherry (red) to mark microtubules and F-actin, respectively, during cleavages. Scale bar: 100 μm. Time: 26 to 49 mpf.

Movie 11:
Related to Figure 3. Time-lapse fluorescence movie (16.5 s interval) of exemplary mini-oocytes expressing Utr-GFP to mark F-actin, obtained from the animal half (left) or vegetal half (right) of an oocyte. Hot-to-cold color coding corresponds to high-to-low actin intensity. Scale bar, 100 μm. Time: 25.5 to 100 mpf.

Movie 12:
Related to Figure 4. High magnification time-lapse fluorescence movie (9 s interval) of the superficial portion of an exemplary oocyte expressing Utr-GFP to mark F-actin . Hot-to-cold color coding corresponds to high-to-low actin intensity. Scale bar, 50 μm. Time: 27 to 39 mpf.

Movie 13:
Related to Figure S5. Time-lapse fluorescence movie (25 s interval) of an exemplary oocyte oocytes expressing Utr-mCherry to mark F-actin (magenta) and Myosin-2-GFP (cyan), illustrating their colocalization during first actin polymerization wave. Scale bars, 50 μm.

Movie 14:
Related to Figure 6. Time-lapse fluorescence movie (4 s interval) of exemplary oocytes expressing Utr-GFP to mark F-actin treated with Cytochalasin B (Cyto B, left) or Jasplakinolide (Jasp, right) during the first two cell cycles. Hot-to-cold color coding corresponds to high-to-low actin intensity. Scale, 100 μm. Time: 25 to 42 mpf.

Movie 15:
Related to Figure 7. Time-lapse fluorescence movie (32 s interval) of an exemplary oocyte expressing Rac1-NGreen to mark ooplasm and yolk granules. Scale bar: 100 μm. Time: 26 to 100 mpf.

Movie 16:
Related to Figure 7. Time-lapse fluorescence movie (32 s interval) of an exemplary oocyte expressing Utr-GFP to mark F-actin (red) and exposed to NileRed to mark yolk granules (green) during the first actin polymerization wave. Scale bar, 100 μ*m* . Time: 25 to 46 mpf.

Movie 17:
Related to Figure 7. Time-lapse fluorescence movie (28 s interval) of an exemplary oocyte expressing Utr-GFP to mark F-actin. Scale bar: 50 μ*m* . Time: 25 to 43 mpf.

Movie 18:
Related to Figure S7. Time-lapse fluorescence movie (2.5 s interval) of an exemplary oocyte expressing Utr-GFP to mark F-actin with additional yolk granules transplanted from a donor oocyte into its blastodisc prior to bulk actin polymerization wave formation. Scale bar, 100 μ*m* . Time: 24 to 41 mpf.

Movie 19:
Related to Figure 7. Time-lapse fluorescence movie (25 s interval) of an exemplary oocyte expressing Utr-GFP to mark F-actin (red) and exposed to NileRed to mark yolk granules (green) during the first actin polymerization wave. Scale bar, 20 μ*m* . Time: 26 to 38 mpf.

Movie 20:
Related to Figure 7. Time-lapse fluorescence movie (60 s interval) of exemplary WT (left) and *Dchs* (Right) oocytes expressing Utr-GFP to mark F-actin. Scale bar, 100 μ*m* . Time: 24 to 73 mpf.

Movie 21:
Related to Figure 7. Time-lapse fluorescence movie (60 s interval) of an exemplary *Dchs* oocyte expressing Utr-GFP to mark F-actin and illustrate incomplete segregation during the first 70 mpf. Scale bar, 100 μ*m* . Time: 24 to 68 mpf.

References

Abraham, V. C., S. Gupta, and R. A. Fluck. 1993. “Ooplasmic Segregation in the Medaka (Oryzias Latipes) Egg.” *The Biological Bulletin* 184 (2): 115–24.

Almonacid, Maria, Wylie W. Ahmed, Matthias Bussonnier, Philippe Mailly, Timo Betz, Raphaël Voituriez, Nir S. Gov, and Marie-Hélène Verlhac. 2015. “Active Diffusion Positions the Nucleus in Mouse Oocytes.” *Nature Cell Biology* 17 (4): 470–79.

Azoury, Jessica, Karen W. Lee, Virginie Georget, Pascale Rassinier, Benjamin Leader, and Marie-Hélène Verlhac. 2008. “Spindle Positioning in Mouse Oocytes Relies on a Dynamic Meshwork of Actin Filaments.” *Current Biology: CB* 18 (19): 1514–19.

Beams, H. W., R. G. Kessel, C. Y. Shih, and H. N. Tung. 1985. “Scanning Electron Microscope Studies on Blastodisc Formation in the zebrafish,Brachydanio Rerio.” *Journal of Morphology* 184 (1): 41–49.

Behrndt, Martin, Guillaume Salbreux, Pedro Campinho, Robert Hauschild, Felix Oswald, Julia Roensch, Stephan W. Grill, and Carl-Philipp Heisenberg. 2012. “Forces Driving Epithelial Spreading in Zebrafish Gastrulation.” *Science* 338 (6104): 257–60.

Bernheim-Groswasser, Anne, Jacques Prost, and Cécile Sykes. 2005. “Mechanism of Actin-Based Motility: A Dynamic State Diagram.” *Biophysical Journal* 89 (2): 1411–19.

Bernheim-Groswasser, Anne, Sebastian Wiesner, Roy M. Golsteyn, Marie-France Carlier, and Cécile Sykes. 2002. “The Dynamics of Actin-Based Motility Depend on Surface Parameters.” *Nature* 417 (6886): 308–11.

Bischof, Johanna, Christoph A. Brand, Kálmán Somogyi, Imre Májer, Sarah Thome, Masashi Mori, Ulrich S. Schwarz, and Péter Lénárt. n.d. “A cdk1 Gradient Guides Surface Contraction Waves in Oocytes.” https://doi.org/10.1038/s41467-017-00979-6.

Borinskaya, Sofya, Katrina B. Velle, Kenneth G. Campellone, Arthur Talman, Diego Alvarez, Hervé Agaisse, Yi I. Wu, Leslie M. Loew, and Bruce J. Mayer. 2016. “Integration of Linear and Dendritic Actin Nucleation in Nck-Induced Actin Comets.” *Molecular Biology of the Cell* 27 (2): 247–59.

Cameron, L. A., M. J. Footer, A. van Oudenaarden, and J. A. Theriot. 1999. “Motility of ActA Protein-Coated Microspheres Driven by Actin Polymerization.” *Proceedings of the National Academy of Sciences of the United States of America* 96 (9): 4908–13.

Chang, Cheng-Chun, Bailin Zhang, Che-Yu Li, Chih-Chien Hsieh, Guillaume Duclos, François Treussart, and Huan-Cheng Chang. 2012. “Exploring Cytoplasmic Dynamics in Zebrafish Yolk Cells by Single Particle Tracking of Fluorescent Nanodiamonds.” In *Advances in Photonics of Quantum Computing, Memory, and Communication V*. https://doi.org/10.1117/12.907181.

Chang, Jeremy B., and James E. Ferrell Jr. 2013. “Mitotic Trigger Waves and the Spatial Coordination of the Xenopus Cell Cycle.” *Nature* 500 (7464): 603–7.

Charras, Guillaume T., Justin C. Yarrow, Mike A. Horton, L. Mahadevan, and T. J. Mitchison. 2005. “Non-Equilibration of Hydrostatic Pressure in Blebbing Cells.” *Nature* 435 (7040): 365–69.

Deneke, Victoria E., Anna Melbinger, Massimo Vergassola, and Stefano Di Talia. 2016. “Waves of Cdk1 Activity in S Phase Synchronize the Cell Cycle in Drosophila Embryos.” *Developmental Cell*. https://doi.org/10.1016/j.devcel.2016.07.023.

Egile, C., T. P. Loisel, V. Laurent, R. Li, D. Pantaloni, P. J. Sansonetti, and M. F. Carlier. 1999. “Activation of the CDC42 Effector N-WASP by the Shigella Flexneri IcsA Protein Promotes Actin Nucleation by Arp2/3 Complex and Bacterial Actin-Based Motility.” *The Journal of Cell Biology* 146 (6): 1319–32.

Ellenberg, J., E. D. Siggia, J. E. Moreira, C. L. Smith, J. F. Presley, H. J. Worman, and J.

Lippincott-Schwartz. 1997. “Nuclear Membrane Dynamics and Reassembly in Living Cells: Targeting of an Inner Nuclear Membrane Protein in Interphase and Mitosis.” *The Journal of Cell Biology* 138 (6): 1193–1206.

Fernández, Juan, Macarena Valladares, Ricardo Fuentes, and Andrea Ubilla. 2006. “Reorganization of Cytoplasm in the Zebrafish Oocyte and Egg during Early Steps of Ooplasmic Segregation.” *Developmental Dynamics: An Official Publication of the American Association of Anatomists*. https://doi.org/10.1002/dvdy.20682.

Field, Christine M., and Péter Lénárt. 2011. “Bulk Cytoplasmic Actin and Its Functions in Meiosis and Mitosis.” *Current Biology: CB* 21 (19): R825–30.

Field, C. M., M. Wuhr, G. A. Anderson, H. Y. Kueh, D. Strickland, and T. J. Mitchison. 2011. “Actin Behavior in Bulk Cytoplasm Is Cell Cycle Regulated in Early Vertebrate Embryos.” *Journal of Cell Science*. https://doi.org/10.1242/jcs.082263.

Fuentes, Ricardo, and Juan Fernández. 2010. “Ooplasmic Segregation in the Zebrafish Zygote and Early Embryo: Pattern of Ooplasmic Movements and Transport Pathways.” *Developmental Dynamics: An Official Publication of the American Association of Anatomists*. https://doi.org/10.1002/dvdy.22349.

Fuentes, Ricardo, Mary C. Mullins, and Juan Fernández. 2018. “Formation and Dynamics of Cytoplasmic Domains and Their Genetic Regulation during the Zebrafish Oocyte-to-Embryo Transition.” *Mechanisms of Development*, August. https://doi.org/10.1016/j.mod.2018.08.001.

Giardini, Paula A., Daniel A. Fletcher, and Julie A. Theriot. 2003. “Compression Forces Generated by Actin Comet Tails on Lipid Vesicles.” *Proceedings of the National Academy of Sciences of the United States of America* 100 (11): 6493–98.

Guevorkian, Karine, Marie-Josée Colbert, Mélanie Durth, Sylvie Dufour, and Françoise Brochard-Wyart. 2010. “Aspiration of Biological Viscoelastic Drops.” *Physical Review Letters* 104 (21): 218101.

Guevorkian, K., and J-L Maître. 2017. “Micropipette Aspiration: A Unique Tool for Exploring Cell and Tissue Mechanics in Vivo.” *Methods in Cell Biology* 139: 187–201.

Hannezo, Edouard, Bo Dong, Pierre Recho, Jean-François Joanny, and Shigeo Hayashi. 2015. “Cortical Instability Drives Periodic Supracellular Actin Pattern Formation in Epithelial Tubes.” *Proceedings of the National Academy of Sciences of the United States of America* 112 (28): 8620–25.

Jermy, Andrew. 2010. “Formin’ a Comet Tail.” *Nature Reviews. Microbiology* 8 (November): 837.

Keren, Kinneret, Patricia T. Yam, Anika Kinkhabwala, Alex Mogilner, and Julie A. Theriot. 2009. “Intracellular Fluid Flow in Rapidly Moving Cells.” *Nature Cell Biology* 11 (10): 1219–24.

Klughammer, Nils, Johanna Bischof, Nikolas D. Schnellbächer, Andrea Callegari, Péter Lénárt, and Ulrich S. Schwarz. 2018. “Cytoplasmic Flows in Starfish Oocytes Are Fully Determined by Cortical Contractions.” *PLoS Computational Biology* 14 (11): e1006588.

Kostyuchenko, R. P., and A. K. Dondua. 2000. “Ooplasmic Segregation and Axis Formation in the polychaeteNereis Virens Embryo.” *Russian Journal of Developmental Biology* 31 (2): 95–105.

Krens, S. F. Gabriel, Jim H. Veldhuis, Vanessa Barone, Daniel Čapek, Jean-Léon Maître, G. Wayne Brodland, and Carl-Philipp Heisenberg. 2017. “Interstitial Fluid Osmolarity Modulates the Action of Differential Tissue Surface Tension in Progenitor Cell Segregation during Gastrulation.” *Development* 144 (10): 1798–1806.

Kwan, Kristen M., Esther Fujimoto, Clemens Grabher, Benjamin D. Mangum, Melissa E. Hardy, Douglas S. Campbell, John M. Parant, H. Joseph Yost, John P. Kanki, and Chi-Bin Chien. 2007. “The Tol2kit: A Multisite Gateway-Based Construction Kit for Tol2 Transposon Transgenesis Constructs.” *Developmental Dynamics: An Official Publication of the American Association of Anatomists* 236 (11): 3088–99.

Leung, Christina F., Sarah E. Webb, and Andrew L. Miller. 1998. “Calcium Transients Accompany Ooplasmic Segregation in Zebrafish Embryos.” *Development, Growth & Differentiation* 40: 313–26.

———. 2000. “On the Mechanism of Ooplasmic Segregation in Single-Cell Zebrafish Embryos.” *Development, Growth & Differentiation*. https://doi.org/10.1046/j.1440-169X.2000.00484.x.

Li-Villarreal, Nanbing, Meredyth M. Forbes, Andrew J. Loza, Jiakun Chen, Taylur Ma, Kathryn Helde, Cecilia B. Moens, et al. 2016. “Dachsous1b Cadherin Regulates Actin and Microtubule Cytoskeleton during Early Zebrafish Embryogenesis.” *Development* 143 (10): 1832.

Maître, Jean-Léon, Hélène Berthoumieux, Simon Frederik Gabriel Krens, Guillaume Salbreux, Frank Jülicher, Ewa Paluch, and Carl-Philipp Heisenberg. 2012. “Adhesion Functions in Cell Sorting by Mechanically Coupling the Cortices of Adhering Cells.” *Science* 338 (6104): 253–56.

Matthews, Helen K., Ulysse Delabre, Jennifer L. Rohn, Jochen Guck, Patricia Kunda, and Buzz Baum. 2012. “Changes in Ect2 Localization Couple Actomyosin-Dependent Cell Shape Changes to Mitotic Progression.” *Developmental Cell* 23 (2): 371–83.

Mayer, Mirjam, Martin Depken, Justin S. Bois, Frank Jülicher, and Stephan W. Grill. 2010. “Anisotropies in Cortical Tension Reveal the Physical Basis of Polarizing Cortical Flows.” *Nature* 467 (7315): 617–21.

Miao, Yansong, Catherine C. L. Wong, Vito Mennella, Alphée Michelot, David A. Agard, Liam J. Holt, John R. Yates Iii, David G. Drubin, and Ronald D. Vale. n.d. “Cell-Cycle Regulation of Formin-Mediated Actin Cable Assembly.” https://doi.org/10.1073/pnas.1314000110.

Mogilner, Alex, and Angelika Manhart. 2018. “Intracellular Fluid Mechanics: Coupling Cytoplasmic Flow with Active Cytoskeletal Gel.” *Annual Review of Fluid Mechanics* 50 (1): 347–70.

Monteith, Corey E., Matthew E. Brunner, Inna Djagaeva, Anthony M. Bielecki, Joshua M. Deutsch, and William M. Saxton. 2016. “A Mechanism for Cytoplasmic Streaming: Kinesin-Driven Alignment of Microtubules and Fast Fluid Flows.” *Biophysical Journal* 110 (9): 2053–65.

Morita, Hitoshi, Silvia Grigolon, Martin Bock, S. F. Gabriel Krens, Guillaume Salbreux, and Carl-Philipp Heisenberg. 2017. “The Physical Basis of Coordinated Tissue Spreading in Zebrafish Gastrulation.” *Developmental Cell* 40 (4): 354–66.e4.

Munjal, Akankshi, and Thomas Lecuit. 2014. “Actomyosin Networks and Tissue Morphogenesis.” *Development* 141 (9): 1789–93.

Munro, Edwin, Jeremy Nance, and James R. Priess. 2004. “Cortical Flows Powered by Asymmetrical Contraction Transport PAR Proteins to Establish and Maintain Anterior-Posterior Polarity in the Early C. Elegans Embryo.” *Developmental Cell* 7 (3): 413–24.

Nance, Jeremy, Edwin M. Munro, and James R. Priess. 2003. “C. Elegans PAR-3 and PAR-6 Are Required for Apicobasal Asymmetries Associated with Cell Adhesion and Gastrulation.” *Development* 130 (22): 5339–50.

Nance, Jeremy, and Jennifer A. Zallen. 2011. “Elaborating Polarity: PAR Proteins and the Cytoskeleton.” *Development* 138 (5): 799–809.

Nishida, Hiroki, Masumi Tokuhisa, and Miyuki Muto. 2017. “Eccentric Position of the Germinal Vesicle and Cortical Flow during Oocyte Maturation Specify the Animal-Vegetal Axis of Ascidian Embryos.” *Mechanisms of Development* 145 (July): S69.

Plastino, Julie, and Cécile Sykes. 2005. “The Actin Slingshot.” *Current Opinion in Cell Biology* 17 (1): 62–66.

Prodon, François, Koichi Hanawa, and Hiroki Nishida. 2009. “Actin Microfilaments Guide the Polarized Transport of Nuclear Pore Complexes and the Cytoplasmic Dispersal of Vasa mRNA during GVBD in the Ascidian Halocynthia Roretzi.” *Developmental Biology* 330 (2): 377–88.

Prodon, François, Christian Sardet, and Hiroki Nishida. 2008. “Cortical and Cytoplasmic Flows Driven by Actin Microfilaments Polarize the Cortical ER-mRNA Domain along the a-v Axis in

Ascidian Oocytes." *Developmental Biology* 313 (2): 682–99.
Prost, J., F. Jülicher, and J-F Joanny. 2015. "Active Gel Physics." *Nature Physics* 11 (February): 111.
Ramanathan, Subramanian P., Jonne Helenius, Martin P. Stewart, Cedric J. Cattin, Anthony A. Hyman, and Daniel J. Muller. 2015. "Cdk1-Dependent Mitotic Enrichment of Cortical Myosin II Promotes Cell Rounding against Confinement." *Nature Cell Biology* 17 (2): 148–59.
Royou, Anne, William Sullivan, and Roger Karess. 2002. "Cortical Recruitment of Nonmuscle Myosin II in Early Syncytial Drosophila Embryos: Its Role in Nuclear Axial Expansion and Its Regulation by Cdc2 Activity." *The Journal of Cell Biology* 158 (1): 127–37.
Sardet, Christian, Alexandre Paix, François Prodon, Philippe Dru, and Janet Chenevert. 2007. "From Oocyte to 16-Cell Stage: Cytoplasmic and Cortical Reorganizations That Pattern the Ascidian Embryo." *Developmental Dynamics: An Official Publication of the American Association of Anatomists* 236 (7): 1716–31.
Satoh, Noriyuki. 1994. *Developmental Biology of Ascidians*. Cambridge University Press.
Schuh, Melina. 2011. "An Actin-Dependent Mechanism for Long-Range Vesicle Transport." *Nature Cell Biology* 13 (12): 1431–36.
Schuh, Melina, and Jan Ellenberg. 2008. "A New Model for Asymmetric Spindle Positioning in Mouse Oocytes." *Current Biology: CB* 18 (24): 1986–92.
Shaner, Nathan C., Gerard G. Lambert, Andrew Chammas, Yuhui Ni, Paula J. Cranfill, Michelle A. Baird, Brittney R. Sell, et al. 2013. "A Bright Monomeric Green Fluorescent Protein Derived from Branchiostoma Lanceolatum." *Nature Methods* 10 (5): 407–9.
Shimizu, T. 1999. "Cytoskeletal Mechanisms of Ooplasmic Segregation in Annelid Eggs." *The International Journal of Developmental Biology* 43 (1): 11–18.
Smutny, Michael, Zsuzsa Ákos, Silvia Grigolon, Shayan Shamipour, Verena Ruprecht, Daniel Čapek, Martin Behrndt, et al. 2017. "Friction Forces Position the Neural Anlage." *Nature Cell Biology* 19 (4): 306–17.
Smutny, Michael, Martin Behrndt, Pedro Campinho, Verena Ruprecht, and Carl-Philipp Heisenberg. 2015. "UV Laser Ablation to Measure Cell and Tissue-Generated Forces in the Zebrafish Embryo in Vivo and Ex Vivo." *Methods in Molecular Biology* 1189: 219–35.
Sommer, Christoph, Christoph Straehle, Ullrich Kothe, and Fred A. Hamprecht. 2011. "Ilastik: Interactive Learning and Segmentation Toolkit." In *2011 IEEE International Symposium on Biomedical Imaging: From Nano to Macro*. https://doi.org/10.1109/isbi.2011.5872394.
Theriot, J. A., T. J. Mitchison, L. G. Tilney, and D. A. Portnoy. 1992. "The Rate of Actin-Based Motility of Intracellular Listeria Monocytogenes Equals the Rate of Actin Polymerization." *Nature* 357 (6375): 257–60.
Thielicke, William, and Eize J. Stamhuis. 2014. "PIVlab – Towards User-Friendly, Affordable and Accurate Digital Particle Image Velocimetry in MATLAB." *Journal of Open Research Software* 2. https://doi.org/10.5334/jors.bl.
Tsai, Tony Y. C., Julie A. Theriot, and James E. Ferrell. 2014. "Changes in Oscillatory Dynamics in the Cell Cycle of Early Xenopus Laevis Embryos." *PLoS Biology*. https://doi.org/10.1371/journal.pbio.1001788.
Valentine, M. T., Z. E. Perlman, T. J. Mitchison, and D. A. Weitz. 2005. "Mechanical Properties of Xenopus Egg Cytoplasmic Extracts." *Biophysical Journal* 88 (1): 680–89.
Velarde, Nathalie, Kristin C. Gunsalus, and Fabio Piano. 2007. "Diverse Roles of Actin in C. Elegans Early Embryogenesis." *BMC Developmental Biology* 7 (1): 142.
Villefranc, Jacques A., Julio Amigo, and Nathan D. Lawson. 2007. "Gateway Compatible Vectors for Analysis of Gene Function in the Zebrafish." *Developmental Dynamics: An Official Publication of the American Association of Anatomists* 236 (11): 3077–87.
Weiser, Douglas C., Richard H. Row, and David Kimelman. 2009. "Rho-Regulated Myosin

Phosphatase Establishes the Level of Protrusive Activity Required for Cell Movements during Zebrafish Gastrulation." *Development* 136 (14): 2375–84.
Westerfield, Monte. 2007. *The Zebrafish Book: A Guide for the Laboratory Use of Zebrafish (Danio Rerio)*.
Wilson, Edmund Beecher. 1900. *The Cell in Development and Inheritance*. The Macmillan Company.
York, Andrew G., Sapun H. Parekh, Damian Dalle Nogare, Robert S. Fischer, Kelsey Temprine, Marina Mione, Ajay B. Chitnis, Christian A. Combs, and Hari Shroff. 2012. "Resolution Doubling in Live, Multicellular Organisms via Multifocal Structured Illumination Microscopy." *Nature Methods* 9 (7): 749–54.

Wilson, Edmund Beecher. 1900. *The Cell in Development and Inheritance*. The Macmillan Company.

KEY RESOURCES TABLE

REAGENT or RESOURCE	SOURCE	IDENTIFIER
Antibodies		
Bacterial and Virus Strains		
Biological Samples		
Chemicals, Peptides, and Recombinant Proteins		
Cytochalasin B	Sigma	Cat# C6762; CAS: 14930-96-2
Nocodazole	Sigma	Cat# M1404; CAS: 31430-18-9
Jasplakinolide	Tocris Bioscience	Cat# 2792; CAS: 102396-24-7
SMIFH2	Sigma	Cat# S4826; CAS: 340316-62-3
CK666	Sigma	Cat# SML0006; CAS: 442633-00-3
DMSO	Sigma	Cat# 276855; CAS: 67-68-5
PD0166285	Abcam	Cat# 219507 ; CAS: 185039-89-8
Dinaciclib	Selleckchem	Cat# S2768 ; CAS: SCH727965
NileRed	ThermoFisher	Cat# N1142; CAS: 7385-67-3
Dextran, Alexa Fluor™ 488; 10,000 MW, Anionic, Fixable	Invitrogen	Cat# D22910
Dextran, Fluorescein, 70,000 MW, Anionic	ThermoFisher	Cat# D1823
Critical Commercial Assays		
Deposited Data		
Experimental Models: Cell Lines		
Experimental Models: Organisms/Strains		
Zebrafish: Tg(actb1:Utr-GFP)	Behrndt et al. 2012	RRID: ZFIN_ZDB-TGCONSTRCT-130206-3
Zebrafish: Tg(actb1:Utr-mCherry)	Behrndt et al. 2012	RRID: ZFIN_ZDB-TGCONSTRCT-130206-3
Zebrafish: Tg(actb1:myl12.1-GFP)	Behrndt et al. 2012	RRID: ZFIN_ ZDB-TGCONSTRCT-130108-2
Zebrafish: Tg(XlEef1a1:dclk2-GFP)	York et al. 2012	RRID: ZFIN_ ZDB-TGCONSTRCT-090707-1
Zebrafish: Tg(actb1:mNeonGreen-Rac1a)	This study	N/A
Zebrafish: dchs1bfh275	Li-Villarreal et al. 2016	RRID: ZFIN_ ZDB-ALT-090715-2
Zebrafish: dchs1bfh275, Tg(actb1:Utr-GFP)	This study	N/A
Oligonucleotides		
Recombinant DNA		

pCS2-Chk1 plasmid for mRNA synthesis	This study	
pCS2-ras-GFP plasmid for mRNA synthesis	Morita et al. 2017	N/A
pCS2-CAMypt plasmid for mRNA synthesis	Smutny et al. 2017	N/A
Software and Algorithms		
Fiji	Schindelin et al., 2012	https://fiji.sc/
Imaris	Bitplane	http://www.bitplane.com/imaris
Excel	Microsoft	https://products.office.com/
GraphPad Prism	GraphPad Software	https://www.graphpad.com/scientific-software/prism/
Matlab	Matlab Software	https://www.mathworks.com/products/matlab.html
Ilastik	Sommer et al. 2011	https://www.ilastik.org/
PIVlab	Thielicke and Stamhuis 2014	https://pivlab.blogspot.com/
Other		

Figure 1

Click here to access/download;Figure;Figure2018_1 resub-01.tif

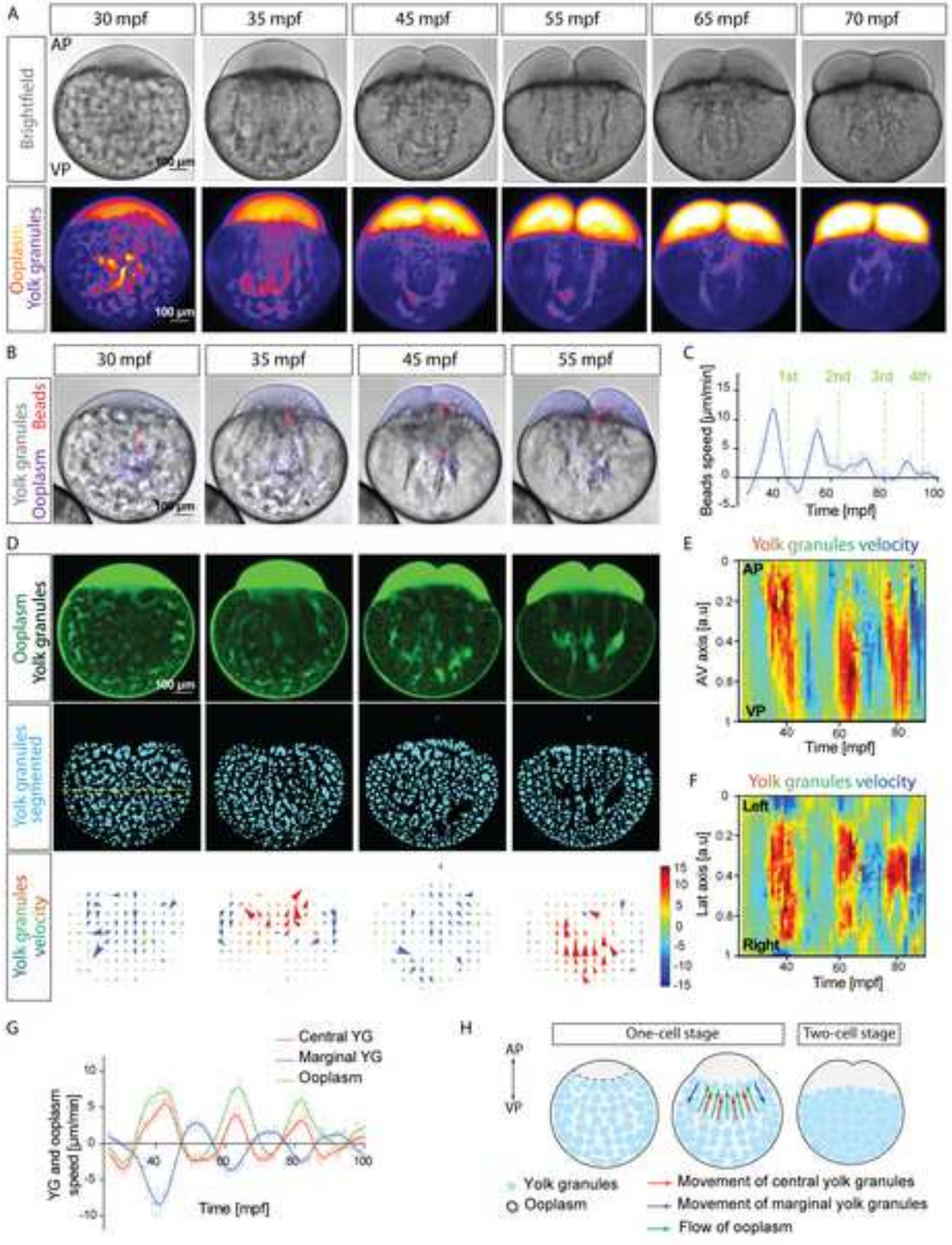

Figure 2

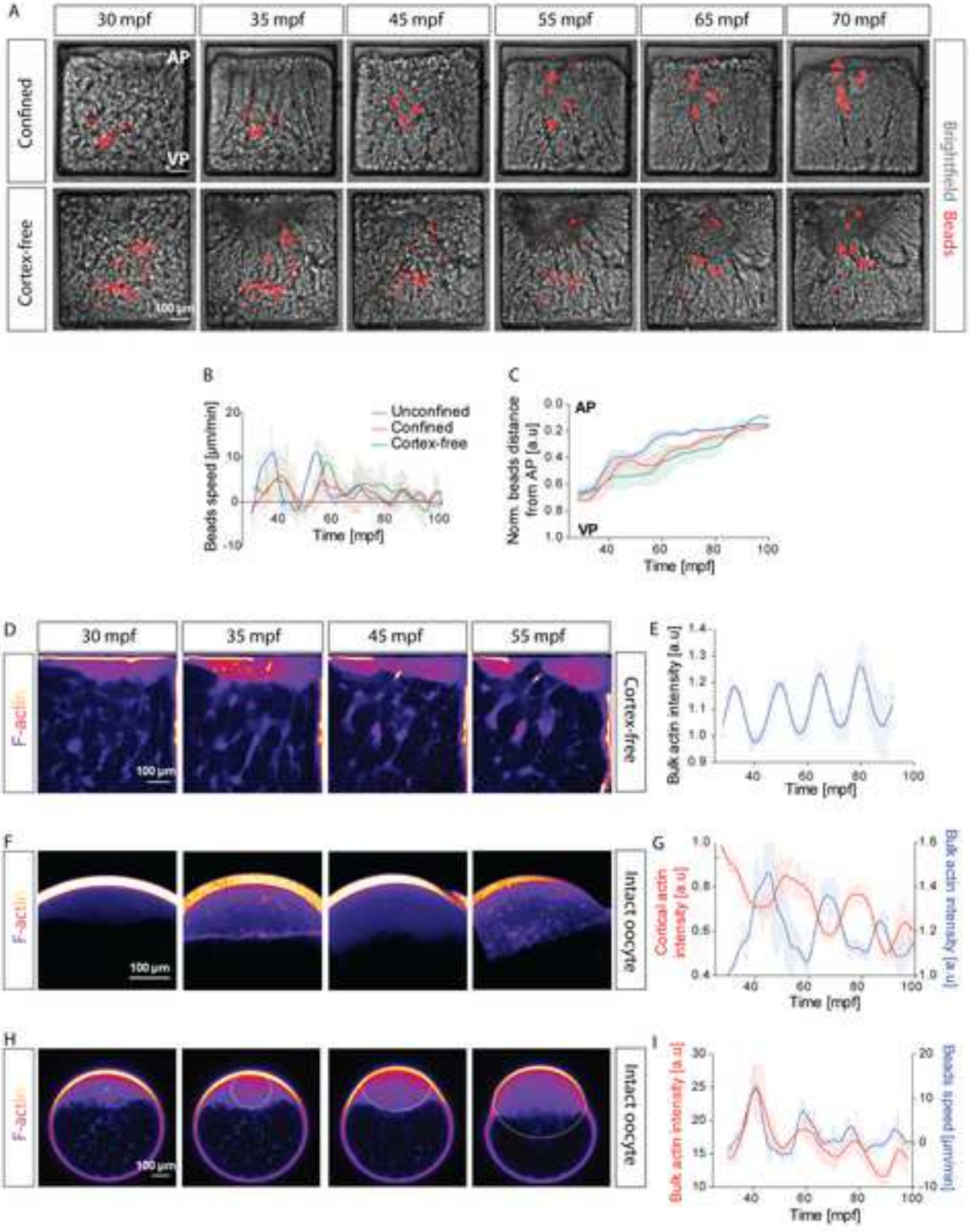

Figure 3

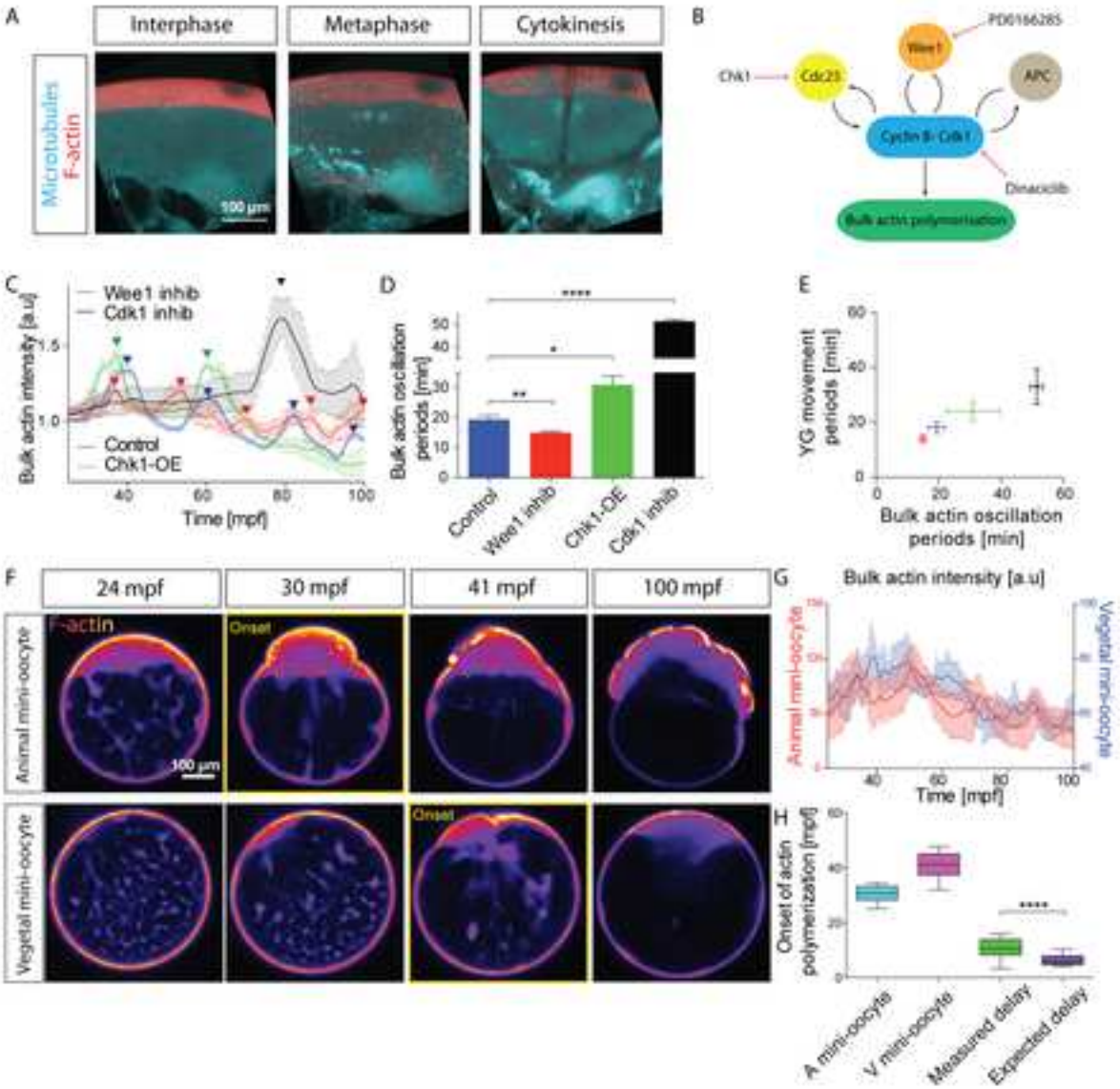

Figure 4

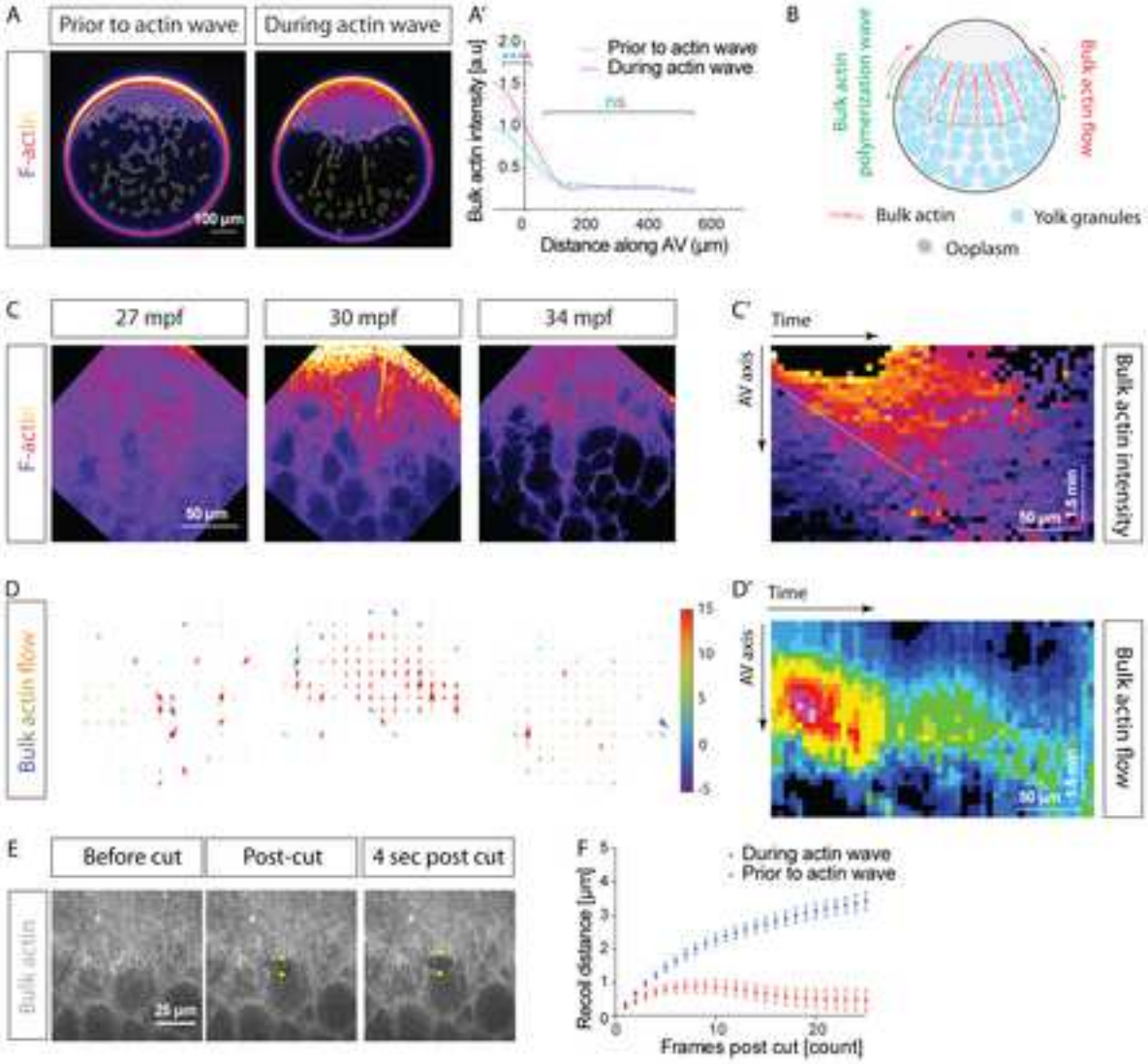

Figure 5

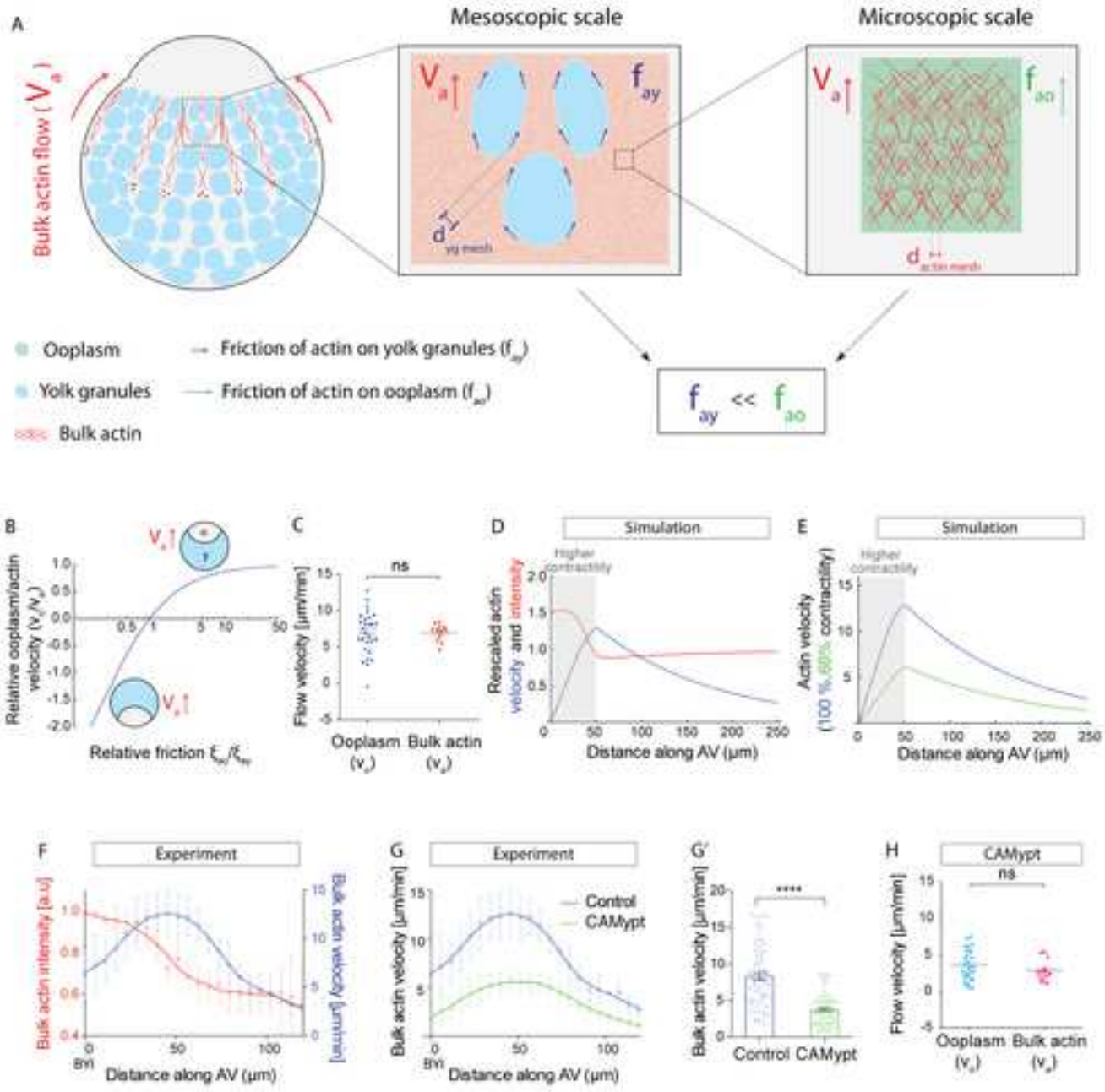

Figure 6

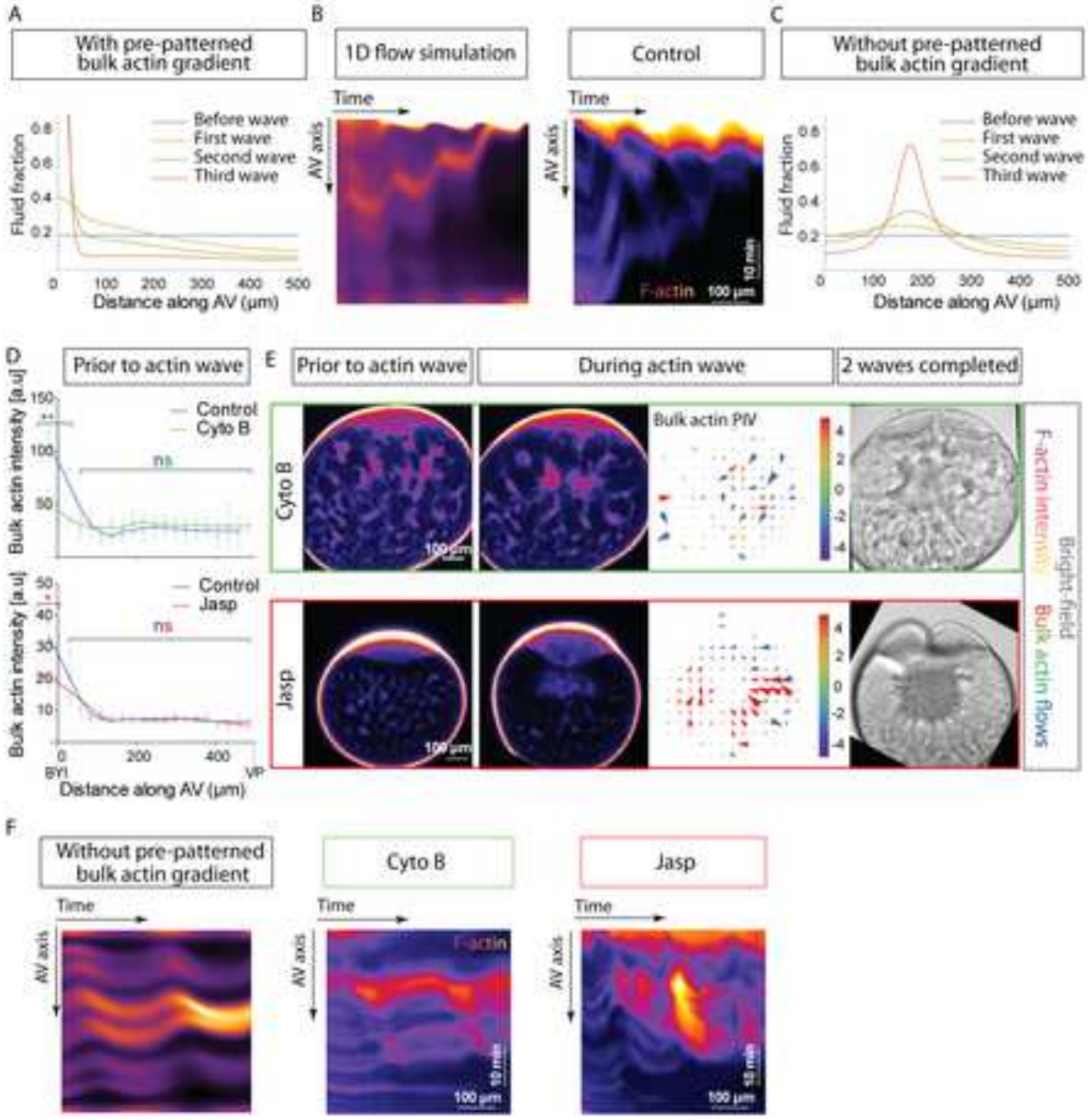

Figure 7

Click here to access/download;Figure;Figure2018_7 resub-01.tif

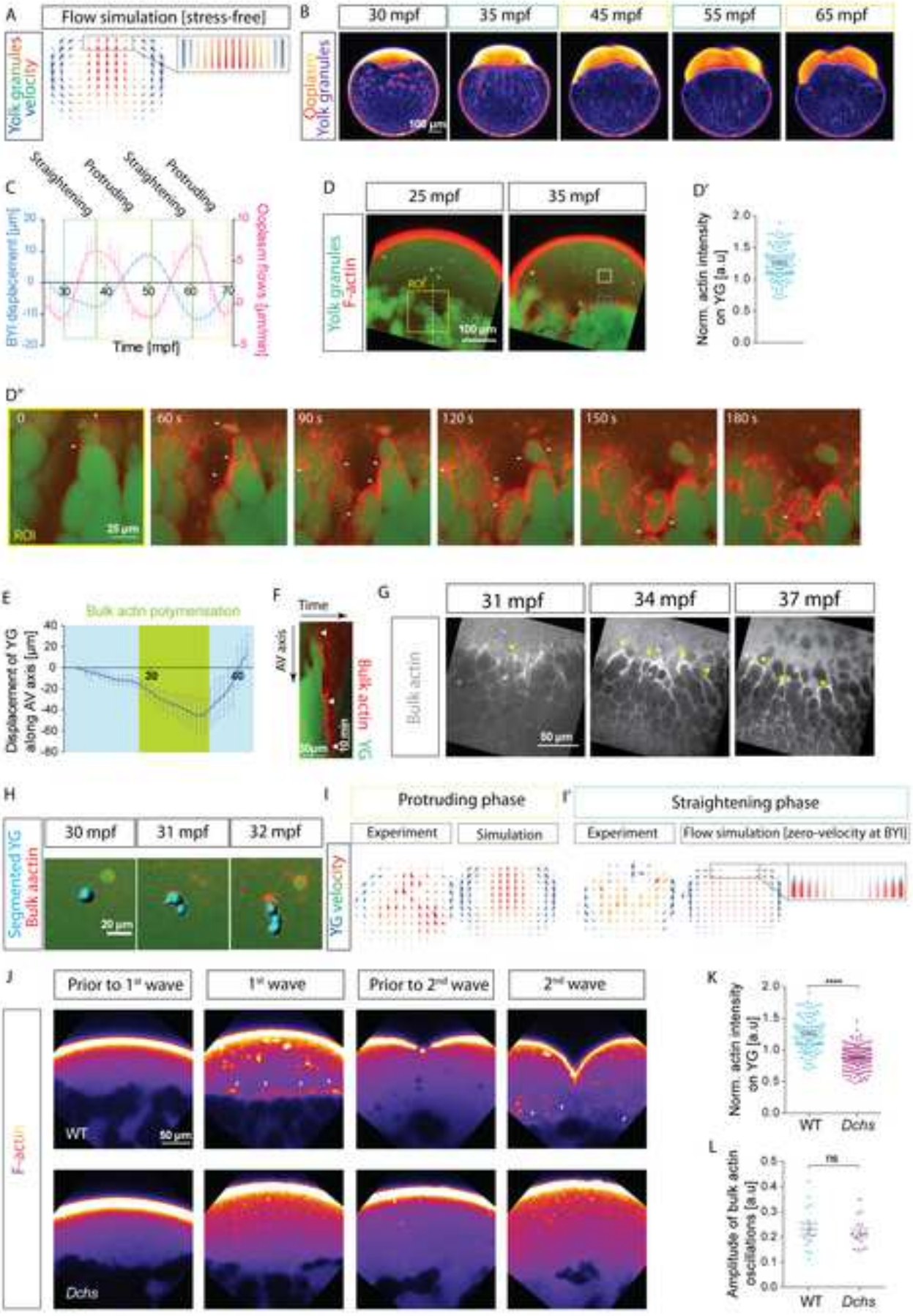

In this Supplementary Theory Note, we provide details on the theoretical approach used to described the mechanics of yolk granule (YG) and fluid/ooplasm segregation, as well as the numerical implementation of the model in one and two dimensions.

1 Three-component hydrodynamics

1.1 Conservation laws

We first write the general constitutive equations for the three-component mixture of actin filaments, fluid and yolk granules, which compose the early embryo. We denote ϕ_a, ϕ_o and ϕ_y respectively the volumetric densities of actin filaments, ooplasmic fluid and yolk granules, adopting a coarse-grained, continuum approach (1, 2), i.e. valid for length scales L at which the yolk granules can be treated as a continuum ($L > 10^1 \mu$m in orders of magnitude). We first write conservation equations for all three phases:

$$\begin{aligned} \partial_t \phi_a + \nabla(v_a \phi_a) &= R(\phi_a, \phi_o, \phi_y) \\ \partial_t \phi_o + \nabla(v_o \phi_o) &= 0 \\ \partial_t \phi_y + \nabla(v_y \phi_y) &= 0 \end{aligned} \tag{1}$$

where we did not include any source terms for the fluid or yolk-granule phase, but a source term for the actin filaments due to polymerisation from a cytoplasmic pool of actin monomers (2). We choose not to model actin monomers explicitly, as they are expected to diffuse fast on the time scales of the processes described here (tens of minutes to hours), and thus lump them with the cytoplasmic fluid phase. We also note that this means we could include this as a source term in the equation for the fluid, however, as $\phi_a \ll \phi_o$ in these systems, this can be neglected and we assume monomeric actin is always in excess. This also allows us not to model explicitly the exchange of monomers between the cortical and bulk actin populations observed in vivo during the oscillatory cycle phase. The components fractions can be thus be related by $\phi_a + \phi_o + \phi_y = 1 \approx \phi_o + \phi_y$.

1.2 Force balance

The next stem is then to write force balance for each three phases, in the absence of inertial effects:

$$\begin{aligned} \nabla.\sigma^a - \phi_a \nabla p &= f_a \\ \nabla.\sigma^o - \phi_o \nabla p &= f_o \\ \nabla.\sigma^y - \phi_y \nabla p &= f_y \end{aligned} \tag{2}$$

where σ^i and f_i are resp. the stress in, and external force applied on, the i phase, with p the pressure which acts as a Lagrange multiplier in the system to ensure incompressibility, and which is weighted by the respective fractions of each phase ϕ_i, as classically assumed in mixture theory citeWeber. We note that an alternative definition would be to include the fractions ϕ within the divergence, although the effects that we consider are at linear order and would thus not be affected by this choice. Finally, we consider that $f_a + f_o + f_y = 0$ (no external forces applied on the system), which is reasonable for the bulk of the oocyte, given our data demonstrating that cortex and oocyte shape changes are dispensable for phase segregation (Figure 2).

1.3 Constitutive equations

Thirdly, we must then specify constitutive relationships for the stresses in each of the three phases.

A first hypothesis for the rheology of the yolk granules would be to consider it elastic, and thus see the fluid exiting the yolk granule phase at the vegetal pole as an example of Terzaghi consolidation, i.e. the classical model of poroelastic fluid flow under external forces (4) (applied

for instance by actin on the boundary between the fluid-YG phases). However, a number of experimental evidences ruled out this hypothesis. Firstly, Terzaghi consolidation would predict a diffusive process on the fluid flow profile within the embryo in time (i.e. that the length scale of fluid flow should increase in time in a diffusive manner). However, this was at odds with the observation of a well-defined length scale of flows from the onset of phase separation (Figure S5J). Secondly, when we probed directly the rheological properties of the YG phase via micropipette aspiration, we found a constant speed of aspiration, consistent with simple newtonian viscosity (Figure S5I-I"). We thus write the stress tensor in the YG phase, modelled as an isotropic simple viscous fluid:

$$\sigma_{ij}^{y} = \frac{\eta_y}{2}(\partial_i v_j + \partial_j v_i) \tag{3}$$

with $\eta_y \approx 30$Pa.s (Figure S5I-I") the viscosity of the YG phase.

For the fluid phase, we also make the classical assumption of isotropic fluid of low viscosity, so that fluid stress simply reduces to the fluid pressure (σ_{ij}^{o} negligible).

Finally, for the actin filament phase, we use the isotropic active gel theory (lumping actin and myosin into a single variable), which we assume to be viscous at such time scales much longer than polymerization/depolymerization (5–9):

$$\sigma_{ij}^{a} = \frac{\eta_a}{2}(\partial_i v_j + \partial_j v_i) + \chi\phi_a\delta_{i,j} \tag{4}$$

where χ is the active contractility arising from actomyosin contraction, η_a the viscosity of the actomyosin gel, and where we linearized the active contraction term $\chi\phi_a$. The sum of all stresses must be equal to the total pressure p_0, given by boundary conditions in 1D.

1.4 External forces

Fourthly, we must specify the functional form of the external forces applied on each phase by the other two, which arises from frictional terms, and thus scales at linear order as the difference between the velocities of each phases

$$\begin{aligned} f_a &= -\xi_{ao}\phi_a\phi_o(v_o - v_a) + \xi_{ay}\phi_a\phi_y(v_a - v_y) \\ f_o &= \xi_{ao}\phi_a\phi_o(v_o - v_a) + \xi_{oy}\phi_o\phi_y(v_o - v_y) \\ f_y &= -\xi_{ay}\phi_a\phi_y(v_a - v_y) - \xi_{oy}\phi_o\phi_y(v_o - v_y) \end{aligned} \tag{5}$$

which suitably sum to zero, and where ξ_i are the friction coefficients between each of the three pairs of components. In principle, both the viscosity and friction coefficients could have more complex dependencies on the fraction of each phase (and thus evolve as a function of phase segregation). However, here, we restrict ourselves to this linear theory, in order to emphasize the core mechanisms of phase segregation.

1.5 Source term on the actin gel

Finally, these equations must be complemented by a functional form for the source term due to actin polymerization/depolymerization. In the simplest case, polymerization and depolymerization in the bulk would not depend on yolk granules, so that $R = -\frac{1}{\tau_a}(\phi_a - \frac{\phi_a^0}{\phi_o^0}\phi_o)$, where the polymerization rate is proportional to the local fraction of fluid (as this dictates monomer availability), and assuming first order kinetics with rate τ_a around an homeostatic density ϕ_a^0.

2 Parameter-fitting and simplifying hypotheses

2.1 Friction coefficients

We now turn to the data to constrain some of the parameters of the model. A key feature of the model is clearly the relative strength of the frictional couplings ξ_i between each phase, which we estimate here.

The frictional coupling ξ_{ao} between fluid and actin polymer is the easiest to estimate, as its classical expression reads $\xi_{ao} = \frac{\eta_o}{l_a^2}$, where η_o is the viscosity of the cytoplasmic fluid permeating the gel, and l_a a characteristic mesh size of the actin gel (2). From the literature, constrained estimates of these parameters can be found as $l_a \approx 40 - 100$nm (10–12) and $\eta_o \approx 10^{-2} - 1$ Pa.s (13–16). However, we sought to constraint this further by measuring the viscosity of the fluid at microscales, by performing FRAP analysis on Dextran molecules of known radius (see Methods and Figure S5F,F' for details), which gave $\eta_o \approx 2.10^{-2}$ Pa.s.

We note that this value matches extremely well with a previously obtained viscosity value in the same system (13), based on nanoparticle tracking ($\eta_o \approx 0.03$ Pa.s), and consistent as well with values for streaming Drosophila oocytes (14). This results in an estimation for the actin-fluid friction coefficient of

$$\xi_{ao} \approx 2.10^{12} - 10^{13} \text{ Pa.s.m}^{-2} \tag{6}$$

Secondly, the frictional coupling ξ_{oy} between fluid and YG phase can be estimated in a similar way as the fluid-actin coupling, by assuming that in the bulk of the embryo, the fluid fraction is small within the YG phase, thus permeating it and leading to $\xi_{oy} = \frac{\eta_o}{l_y^2}$, where l_y is the characteristic mesh size of the YG phase. From the data $l_y \approx 15\mu$m (Figure S5H), leading to a friction coefficient 4-6 orders of magnitude below ξ_{ao}:

$$\xi_{oy} \approx 10^{8} \text{ Pa.s.m}^{-2} \tag{7}$$

The frictional coupling ξ_{ay} between the actin gel and the YG phase is slightly harder to estimate, as it depends on the exact nature of the interactions between the two phases (and whether for instance the actin gel can be seen as a simple fluid permeating the YG phase, without specific attachment or repulsion to it). Making this assumption to get orders of magnitude leads $\xi_{ay} = \frac{\eta_a}{l_y^2}$, with η_a the viscosity of the cytoplasmic actin gel. Again, as this is an essential part of the model, we sought to measure this viscosity, which needs to be measured at the mesoscale (i.e. at length scales much larger than the mesh size of F-Actin gels). We thus resorted to micropipette aspiration in the blastodisk (which is clear of yolk granules, simplifying the analysis), during the process of phase segregation, and at short-time scales (1 min) relevant for the time scales of F-Actin flows in vivo. These measurements were consistent with a Newtonian fluid, with a viscosity three orders of magnitude larger than the fluid (see Methods and Figure S5G,G' for details), and gave us an estimate of $\eta_a \approx 40 Pa.s$. Interestingly, our estimates, at the micro- and meso-scales, are within similar orders of magnitude from classical rheological measurements of cytoplasmic extracts from Xenopus eggs (17) (which measured a fluid viscosity at microscales of 20 mPa.s, and F-Actin-dependent mesoscopic viscosity of the egg of order $1 - 5$ Pa.s). However, to confirm that the viscosity we were measuring did come from the actin cytoskeleton, we repeated these experiments in embryos treated with Cyto B (which interferes with the actin cytoskeleton). Importantly, this resulted in a drastic reduction of the measured viscosity (Figure S5G',G''), consistent with a key rheological contribution of F-actin in the experiment.

Combined, these measurements provide an estimate for the friction coefficient:

$$\xi_{ay} \approx 4.10^{11} \text{ Pa.s.m}^{-2} \tag{8}$$

which is interestingly, intermediate between the two other friction coefficients, although still at least an order of magnitude smaller than the lower bound of ξ_{ao}.

One should note however that this estimate of ξ_{ay} should be seen as a conservative upper-bound. Indeed, the interactions between polymers and surfaces often involve the formation of low-viscosity boundary layers of fluid, which tend to diminish the effective interaction. Consistent with this, we find that the actin velocity does not vanish at the boundary with yolk-granules (Figure 4C and Movie 9), indicative that classical no-slip boundary conditions from simple fluids are not valid, and consistent with a lower effective friction ξ_{ay} compared to the estimate above.

These orders of magnitude suggest that fluid and actin gels will tend to move together, given that their friction coefficient is larger than the other interactions.

2.2 Limiting case of negligible actin-granule friction

To give additional insights into the dynamics, we first consider the limiting case, where the frictional force on actin f_a is small compared to the other forces acting on the actin gel (i.e. vs. the active and viscous stresses). This is motivated by the fact that actin flows propagate over very long distances, of order of the embryo size, arguing for a large hydrodynamical length for the actin gel.

This case is particularly convenient, as the equations for actin decouple from the rest of the system, and becomes a variation of a Keller-Segel model of active fluid (6):

$$\begin{aligned} \partial_t \phi_a + \nabla.(v_a \phi_a) &= -\frac{\phi_a - \phi_a^0 \phi_o}{\tau_a} + D_a \Delta \phi_a \\ \eta_a \Delta v_a - \chi_a \nabla \phi_a &= 0 \end{aligned} \tag{9}$$

which displays a contractility-driven instability, leading to large scale actin flows (on the length scale of the system size). Note that we added a small diffusive flux with coefficient D_a, which does not impact the key features of the resulting dynamics, but is required for stability viz. high wavenumber modes (6). In turn, this non-zero actin velocity v_a imposes a frictional force $F_a(x)$ on both the fluid and YG phases. Moreover, in 1D, the equations are drastically simplified by the fact that the conservation of phases ($\phi_o + \phi_y \approx 1$), coupled with no-flux/clamped boundary conditions can be translated, by combining it with the conservation equation and integrating once, into a relationship between speeds of fluid and YG: $\phi_o v_o \approx -\phi_y v_y$, i.e. the global barycentric velocity is zero in the system. In 2D, one only gets $\nabla.(\phi_o v_o + \phi_y v_y) = 0$, which allows for instance for vorticity (see two-dimensional numerical integration of Figure 7). One can then subtract the force balance on the fluid and YG to eliminate the pressure terms, yielding:

$$\eta_y \Delta v_y - \phi_a \phi_y \xi_{ao} (v_a + \frac{\phi_y}{1-\phi_y} v_y) = \xi_{ay} \phi_a \phi_y (v_y - v_a) \tag{10}$$

Assuming a 1D domain $x \in [0, L]$, with $v_y(0) = 0$ (no flux in the vegetal pole), $\sigma^y(L) = 0$ (zero stress at the yolk-granule-blastodisk interface), and a constant F-Actin velocity v_a, combined with $v_y = \phi_o / \phi_y v_o$, we can obtain an analytical form for the fluid and granule velocity:

$$v_y = -v_a \phi_o \frac{\xi_{ao} - \xi_{ay}}{\phi_y \xi_{ao} + \phi_o \xi_{ay}} \left(\frac{\cosh \frac{L-x}{l}}{\cosh \frac{L}{l}} - 1 \right) \tag{11}$$

which converges, on a hydrodynamical length scale $l = \sqrt{\frac{\xi_t}{\eta_y}}$ (where we defined the global friction coefficient $\xi_t = \frac{\phi_a \phi_y}{\phi_o}(\phi_y \xi_{ao} + \phi_o \xi_{ay})$) on a constant solution (plotted on Figure 5B):

$$v_y = -v_a \phi_o \frac{\xi_{ao} - \xi_{ay}}{\phi_y \xi_{ao} + \phi_o \xi_{ay}} \tag{12}$$

and

$$v_o = v_a \phi_y \frac{\xi_{ao} - \xi_{ay}}{\phi_y \xi_{ao} + \phi_o \xi_{ay}} \tag{13}$$

meaning that the fluid flows together with the actin if and only if the fluid-actin friction coefficient is larger than the YG-actin friction coefficient. We recover the familiar limits of $v_o = v_a$ if $\xi_{ao} \gg \xi_{ay}$, and $v_o = -\phi_y/\phi_o v_a$ (which corresponds to $v_y = v_a$) if $\xi_{ao} \ll \xi_{ay}$.

In the relevant regime here of $\xi_{ao} \gg \xi_{ay}$, this means that the frictional forces acting on actin can be calculated as

$$f_a = -\phi_a v_a \frac{\xi_{ao}\xi_{ay}}{\phi_y \xi_{ao} + \phi_o \xi_{ay}} \tag{14}$$

which corresponds to the geometric mean of the two friction coefficients acting on actin filaments. Given that we have deduced, from orders of magnitude in the section above, that $\xi_{ao} \gg \xi_{ay}$, this expression simplifies to:

$$f_a = -\frac{\phi_a}{\phi_y} v_a \xi_{ay} = \xi_{eff} v_a \tag{15}$$

i.e. that the actin network experiences a friction from the YG only, given that F-actin drags the ooplasm along. Although, for the reasons mentioned above, the effective YG-actin friction ξ_{ay} is hard to estimate precisely, we will thus fit it from the data, as the theory predicts that the F-actin/fluid velocity profile should decay exponentially with a characteristic length scale λ:

$$\lambda \approx \sqrt{\frac{\eta_a}{\xi_{ay}}} \tag{16}$$

This fitted well with the experimental data for the ooplasm speed profile during the first wave (Figure S5J), allowing us to infer the length scale $\lambda \approx 160 \pm 13 \mu$m (we found similar values in the range of $150 - 200 \mu m$ for the subsequent waves). From the measurements above of $\eta_a \approx 40$ Pa.s, this pins the effective YG-actin friction coefficient to a value which is two-orders of magnitude smaller than estimated from an ideal permeating fluid assumption:

$$\xi_{ay}^{eff} \approx 10^9 \text{ Pa.s.m}^{-2} \tag{17}$$

We will thus used this inferred value of ξ_{ay} in all the rest of this Theory Note.

2.3 Numerical integrations of the model in 1D for wild-type oocytes

We thus simulated in one-dimension Eq. 9, together with the conservation equation Eq. 1 for the fluid phase. As we are interested primarily in the bulk mechanisms of phase separation, we take clamped, no-flux boundary conditions on both the blastodisk-yolk-granule interface and vegetal pole. From our measurements, we set $L = 500 \mu m$ the size of the egg and $\phi_o^0 = 0.2$ the initial fraction of fluid in the bulk of the oocyte (Figure 1A,4A and 6E), as well as $\xi_{ay}^{eff} = 10^9$ Pa.s.m^{-2} and $\eta_a = 40$ Pa.s from the measurements described above. We also assumed $\tau_a \approx 30$ s from past orders of magnitude (11), and $D_a \approx 1 \mu m^2.s^{-1}$ (required for stability, although we performed a sensitivity analysis to check that this value had little effect on the dynamics when increasing or decreasing it by an order of magnitude). These values can be rationalized as they yield a length scale of $\sqrt{D_a \tau_a} \approx 5 \mu m$ in the conservation equation, comparable to filament size.

We then performed numerical integration of these equations with a spatiotemporal varying contractility $\chi(x,t) = \chi_{max} f(x/L - t/T)$, i.e. a propagating wave of contractility (chosen sinusoidal) with the measured period $T = 17$min (see Figure 3), for different values of maximal contractility χ_{max}. As the characteristic velocity of F-Actin flows is around $v_a \approx 10 \mu m.min^{-1}$, we found that values around $\chi_{max} = 0.1 - 0.5$Pa yielded realistic velocity profiles (Figure S6C,E), with the simulations of Figure 6 and Figure S6 performed with $\chi_{max} = 0.2$Pa). One should note that this value of contractility is very low compared to measurements from cortical F-actin (as was the case for the viscosity that the bulk F-actin phase inferred from aspiration experiments), which might have to do with the specific architecture of filaments in the cortex.

Nevertheless, this value of χ_{max} can also be drastically constrained from the laser-ablation data. Indeed, numerical integration of the mechanical part of Eq. 9, where F-Actin concentration is a Heaviside function (to mimic a localized laser ablation severing the actomyosin network) predicts an instantaneous recoil velocity profile decaying on the length scale $\sqrt{\eta_a \xi_{ay}}$, and with maximal speed $v_{max} = \frac{\chi}{2\eta_a \xi_{ay}}$. As we measured $v_{max} \approx 1 \mu m.s^{-1}$ during the peak of the actomyosin wave in the egg (Figure S1E,F), this predicts

$$\chi_{max} \approx 0.4 Pa \tag{18}$$

in good quantitative agreement with the values inferred from fitting the velocities of F-Actin flows during the segregation process.

It should be noted that we have modelled the traveling F-actin wave as a contractility wave here, based on the laser-cut experiments of Figure 4E,F showing that contractility increased during the wave, from values close to zero prior to the wave. This neglects the fact that the wave also locally increases F-Actin concentration itself. However, as we have pooled F-actin and MyosinII in a single variable within our descriptions, the approximation is warranted, and we have verified that adding a polymerization component to the wave does not change qualitatively our findings.

Finally, we perform the numerical simulations for wild-type oocyte taking into account a spatially graded actin polymerization $R = \frac{1}{\tau_a}(\phi_a^0 \frac{\phi_o}{\phi_o^0}) f(x) - \phi_a)$, described by a function $f(x) = 1 + ae^{-x/\lambda}$ and fitted from Figure 4A,A' (with $a \approx 1$ and $\lambda \approx 100 \mu$m). Importantly, this leads to robust ooplasm accumulation at the animal pole within a few oscillation cycles (Figure 6A and Figure S6C-C'), and reproduces the experimental phenomenology of depleting first the regions closest to the animal pole, before pulling it more distant regions gradually. To account for the noisy profile of fluid fraction observed initially experimentally, we also added noise to our initial conditions, to examine the influence on the resulting segregation dynamics. Strikingly, this reproduced well the data, with gradual coalescence on neighboring fluid accumulation, and a subsequent and gradual oscillating movements of ooplasm-rich regions towards the animal pole (Figure 6B).

2.4 Numerical integrations of the model in 1D for drug treatments

Finally, in order to model drug treatment as well, and in particular to mimic Cytochalasin B or Jasplakinolide treatment (Figure 6C-E and Figure S6), where the pre-patterned bulk actin gradient is reduced, we performed the same simulations, keeping all parameters constant except setting $a = 0$ (no pre-patterned actin gradient). Simulations without noise revealed a progressive accumulation of ooplasm and F-actin towards the center of the oocyte (Figure 6C and Figure S6E,E'), while adding noise again gave rise to a similar phenotype of progressive coarsening of ooplasm/actin accumulation (Figure 6F). Again, plotting these simulations as kymographs revealed good agreement with the data (Figure 6F). Depending on the initial conditions, one could also observed partial accumulation of ooplasm at the animal pole (together with the formation of central pockets), something that was also observed experimentally in drug treatments (Figure 6E).

To be more systematic in understanding the influence of a pre-patterned gradient on phase segregation, we performed a sensitivity analysis on parameter a (relative strength/amplitude of the gradient). We thus did a parameter sweep in a, performing for each value 50 numerical simulations (starting each time from different random initial conditions, and keeping all other parameter constant). We then computed after three numerical oscillations of F-Actin how much cytoplasm had been transported in animal pole, by numerically calculating the fraction of oocyte $\phi_{ani}^o = \int_0^{l_{ani}} \phi_o(x,T)dx / \int_0^L \phi_o(x,T)dx$, where l_{ani} is the size of the animal pole (which we approximated as $L/20$, although the exact value does not influence the findings). Results are presented in Figure S6A. Importantly, this demonstrated that for wild-type, accumulation of ooplasm at the animal pole was rather insensitive to the exact amplitude of the pre-patterned gradient a, as even moderate values of pre-patterning gradients are enough to robustly bias the dynamics of fluid towards the animal pole. However, this confirmed that for lower values of gradient amplitude, animal localization

of ooplasm is lost. Interestingly, turning back to the data, we found that Jasplakinolide treatment resulted in a milder change in the pre-patterned gradient than Cytochalasin B. We then sought to check whether this would translate, as we would predict, in differences in ooplasm localization by quantifying more Jasplakinolide-treated embryos (Figure S6D). Importantly, we found that the Jasplakinolide phenotype was in fact intermediate, with around 70% of embryos showing a central ooplasm pocket (as in Cytochalasin treatment), while around 30% of embryos showed a ooplasmic pocket closer to the animal pole. In contrast, in wild-type (resp. in Cytochalasin), the ooplasm accumulation was always located in the animal pole (resp. the center) of the oocyte (Figure S6D). Finally, because robust localization still occurs in confined embryos (Figure 2A-E), we verified that the pre-patterned actin gradient was still present in this condition (Figure S5A). Because confined embryos have flat surfaces, this further strengthened our confidence that the gradient was not an imaging artifact from the spherical geometry of the embryo (a conclusion confirmed by the disappearance of the gradient in Cytochalasin B treatment despite the absence of geometrical or compositional changes in the oocyte). Together, these analyses therefore strengthened the link between F-actin pre-patterned gradients and ooplasm localisation.

Finally, to model the effect of changing contractility (downregulation in the case of the CA-Mypt experiment), we also tested how the velocities profiles were modified during the first wave when either increasing or decreasing contractility χ_{max} by 40%. As expected, halving contractility had the effect of nearly halving the velocity profiles (Figure 5E), as in the experimental comparison of WT vs. CA-Mypt (Figure 5G,G').

As a whole, this analysis demonstrates that contractility-drive actomyosin flows in a multiphasic medium can be used to drive phase segregation in a generic way via the differential friction of actomyosin networks on each phase of the system. We further constraint the parameters of the theory to demonstrate that this mechanism explain the observed spatiotemporal dynamics of phase segregation.

2.5 Numerical integrations of the model in 2D

To numerically integrate the model in two-dimensions, we used a finite element methods (via the Freefem+ software). However, we made a number of simplifying assumptions to provide insights into the swirling dynamics observed in yolk granules. In particular, given the results of the one-dimensional model (see above), we grouped F-actin and fluid into a single phase, and concentrated solely on the static solution of the Stokes equation describing the yolk-granule phase (viscosity η_y, with steady state friction force from the F-actin/fluid velocity $v_a(x,y)$, taking x along the animal-vegetal axis and y its perpendicular). Guided by the results described above, we took the functional form $v_a(x,y) = v_m e^{-x/l} e^{-y^2/2/s^2}$, with v_m setting the scale of velocities, l the hydrodynamical length of velocity decay (inferred as mentioned above from Figure S5J). Moreover, as discussed in the main text, we found that the fraction of fluid and F-actin initially in the egg was larger towards the center of the egg ($y = 0$, see Figure 4A), which we model as a Gaussian center around the egg center and of width inferred at $s \approx 200 \mu m$. This means that the yolk granules will experience larger frictional forces in the center of the egg, which leads generically in 2D to swirling motions.

Figure 7A and 7I (right panel) displays a numerical integration of the granule velocity profile for $v_y = 0$ boundary conditions around the egg, and $\sigma^y = 0$ at the blastodisk yolk-granule interface (BYI). Such a boundary condition at the BYI is motivated by the fact that there can be a non-zero velocity at such a fluid-fluid interface, contrary to around the egg cortex. This leads to positive velocities in the center of the BYI and negative velocities in its periphery, closely mirroring experimental data of Figure 7I (left panel). However, as discussed in the main text, such a stress-free condition might not generically hold, in particular in the presence of extensive F-actin comet formation at the interface, which is expected to rigidify it and act as a corset preventing yolk granules to pass while allowing fluid movement. As a detailed description of the mechanics and

spatiotemporal dynamics of the interface is out-of-scope of this work, we simplified the problem by describing this as imposing a zero net velocity on the BYI (i.e. inwards movements of granules locally matching the outwards movements of fluid). By construction, this prevents gradients of velocities to form at the interface (in contrast to the stress-free case), and causes a stagnation point for velocities of yolk granules away from the interface (see Figure 7I, right panel for a simulation). Again, this closely matched the data of Figure 7I (left panel)

Together, this demonstrates that extending the model in two-dimensions can capture key elements of the complex spatiotemporal dynamics of yolk-fluid segregation post-fertilisation.

References

1. Callan-Jones, A.C. and Julicher, F., 2011. Hydrodynamics of active permeating gels. New Journal of Physics, 13(9), p.093027.

2. Mogilner, A. and Manhart, A., 2018. Intracellular fluid mechanics: Coupling cytoplasmic flow with active cytoskeletal gel. Annual Review of Fluid Mechanics, 50, pp.347-370.

3. Weber, C.A., Rycroft, C.H. and Mahadevan, L., 2018. Differential Activity-Driven Instabilities in Biphasic Active Matter. Physical Review Letters, 120(24), p.248003.

4. Biot, M.A., 1941. General theory of three-dimensional consolidation. Journal of applied physics, 12(2), pp.155-164.

5. Joanny, J.F. and Prost, J., 2009. Active gels as a description of the actin-myosin cytoskeleton. HFSP journal, 3(2), pp.94-104.

6. Hannezo, E., Dong, B., Recho, P., Joanny, J.F. and Hayashi, S., 2015. Cortical instability drives periodic supracellular actin pattern formation in epithelial tubes. Proceedings of the National Academy of Sciences, 112(28), pp.8620-8625.

7. Recho, P., Putelat, T. and Truskinovsky, L., 2013. Contraction-driven cell motility. Physical review letters, 111(10), p.108102.

8. Saha, A., Nishikawa, M., Behrndt, M., Heisenberg, C.P., Julicher, F. and Grill, S.W., 2016. Determining physical properties of the cell cortex. Biophysical journal, 110(6), pp.1421-1429.

9. Prost, J., Julicher, F. and Joanny, J.F., 2015. Active gel physics. Nature Physics, 11(2), p.111.

10. Charras, G. T., Yarrow, J. C., Horton, M. A., Mahadevan, L., and Mitchison, T. J. (2005). Non-equilibration of hydrostatic pressure in blebbing cells. Nature, 435(7040), 365.

11. Salbreux, G., Charras, G., and Paluch, E. (2012). Actin cortex mechanics and cellular morphogenesis. Trends in cell biology, 22(10), 536-545.

12. Eghiaian, F., Rigato, A., and Scheuring, S. (2015). Structural, mechanical, and dynamical variability of the actin cortex in living cells. Biophysical journal, 108(6), 1330-1340.

13. Chang, C.C., Zhang, B., Li, C.Y., Hsieh, C.C., Duclos, G., Treussart, F. and Chang, H.C., 2012, February. Exploring cytoplasmic dynamics in zebrafish yolk cells by single particle tracking of fluorescent nanodiamonds. In Advances in Photonics of Quantum Computing, Memory, and Communication V (Vol. 8272, p. 827205). International Society for Optics and Photonics.

14. Monteith, C.E., Brunner, M.E., Djagaeva, I., Bielecki, A.M., Deutsch, J.M. and Saxton, W.M., 2016. A mechanism for cytoplasmic streaming: Kinesin-driven alignment of microtubules and fast fluid flows. Biophysical journal, 110(9), pp.2053-2065.

15. Ganguly, S., Williams, L.S., Palacios, I.M. and Goldstein, R.E., 2012. Cytoplasmic streaming in Drosophila oocytes varies with kinesin activity and correlates with the microtubule cytoskeleton architecture. Proceedings of the National Academy of Sciences, 109(38), pp.15109-15114.

16. Daniels, B.R., Masi, B.C. and Wirtz, D., 2006. Probing single-cell micromechanics in vivo: the microrheology of C. elegans developing embryos. Biophysical journal, 90(12), pp.4712-4719.

17. Valentine, M. T., Perlman, Z. E., Mitchison, T. J., and Weitz, D. A. (2005). Mechanical properties of Xenopus egg cytoplasmic extracts. Biophysical Journal, 88(1), 680-689.

Supp. Figure 1

Click here to access/download;Supplemental Figure;Supfigure2018_1-01.tif

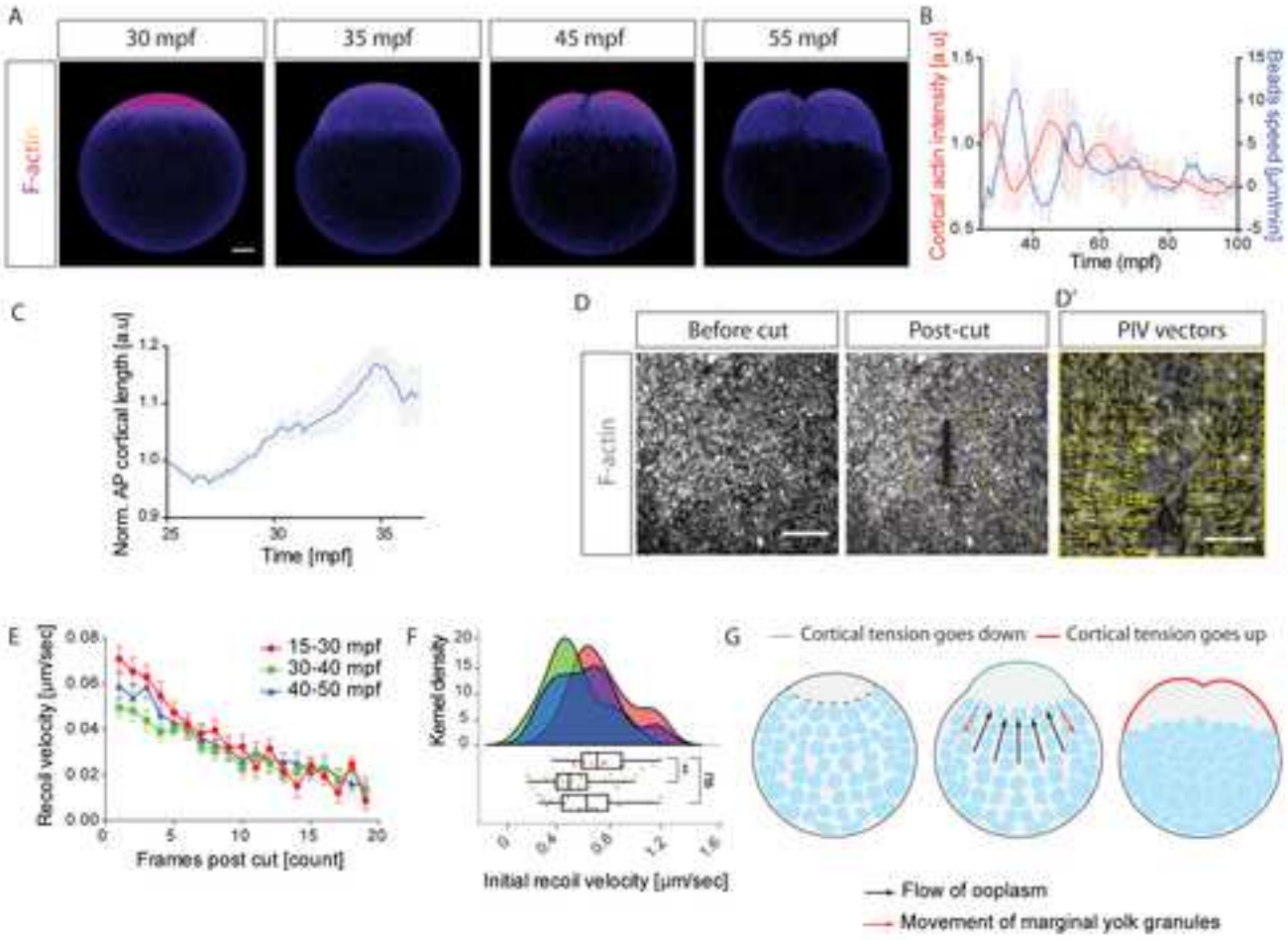

Supp. Figure 2

Click here to access/download;Supplemental Figure;Supfigure2018_2-01.tif

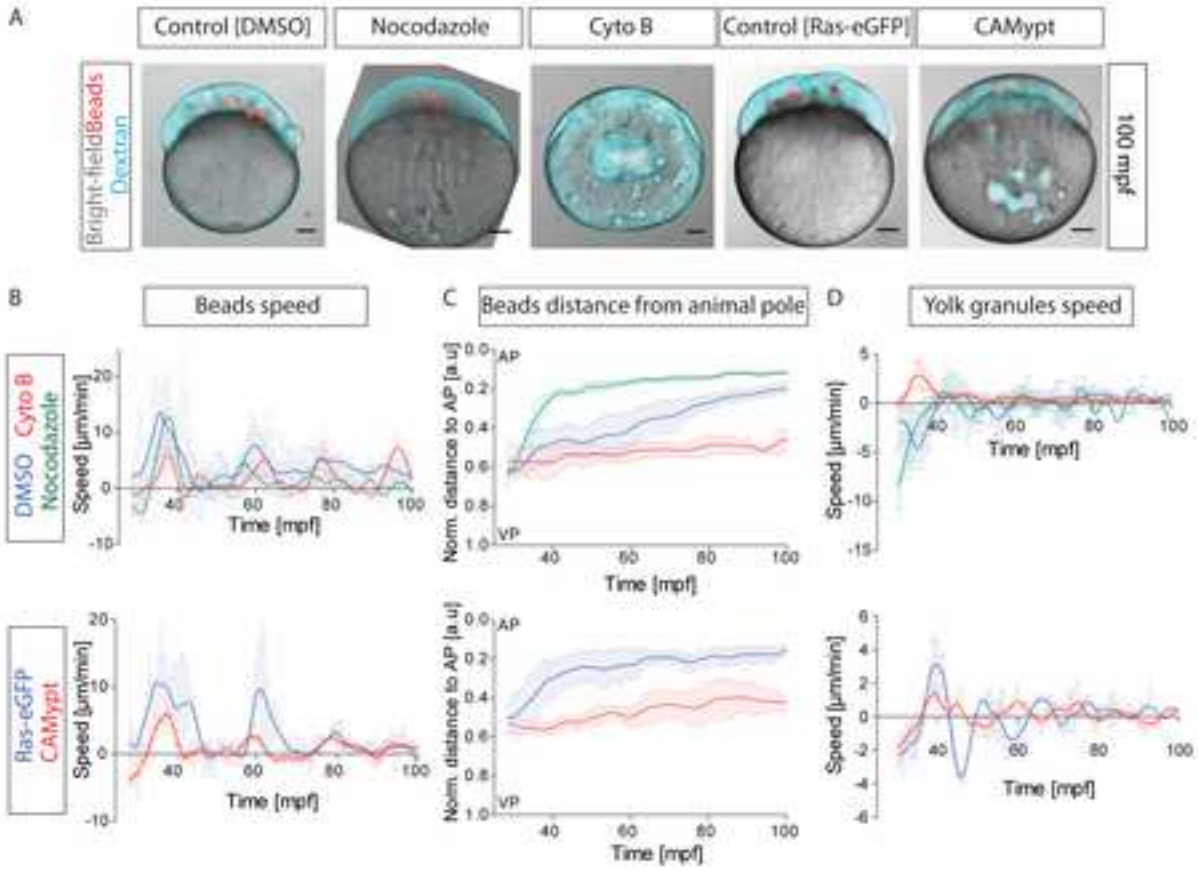

Supp. Figure 3

Click here to access/download;Supplemental Figure;Supfigure2018_3-01.tif

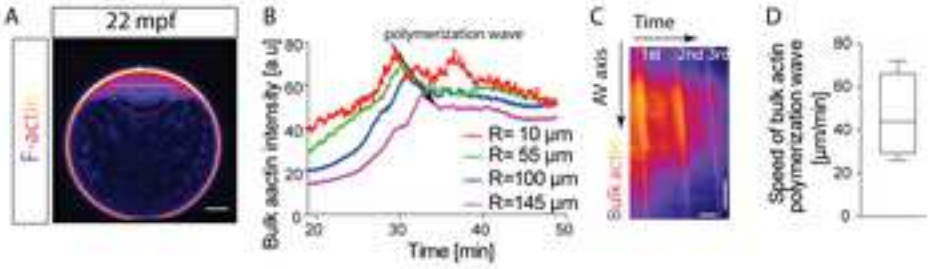

Supp. Figure 4

Click here to access/download;Supplemental Figure;Sup figure2018_4-01.tif

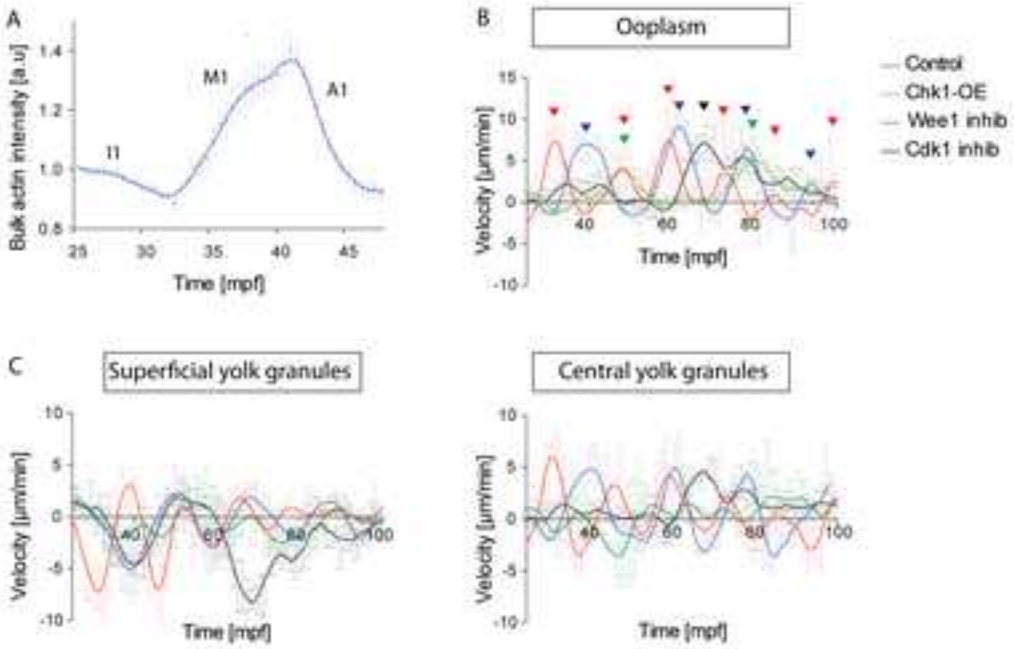

Supp. Figure 5

Click here to access/download;Supplemental Figure;Supfigure2018_5-01.tif

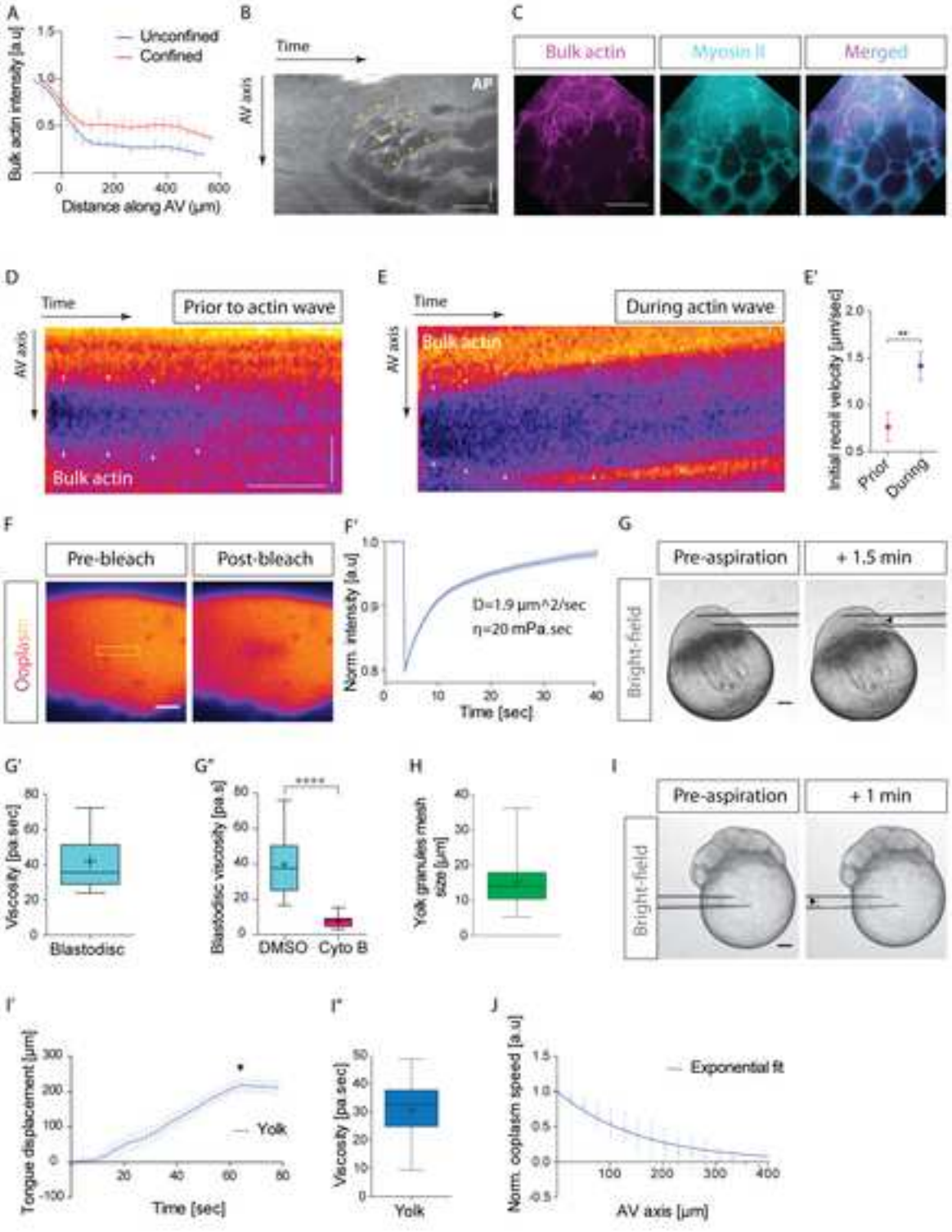

Supp. Figure 6

Click here to access/download;Supplemental Figure;Supfigure2018_6-01.tif

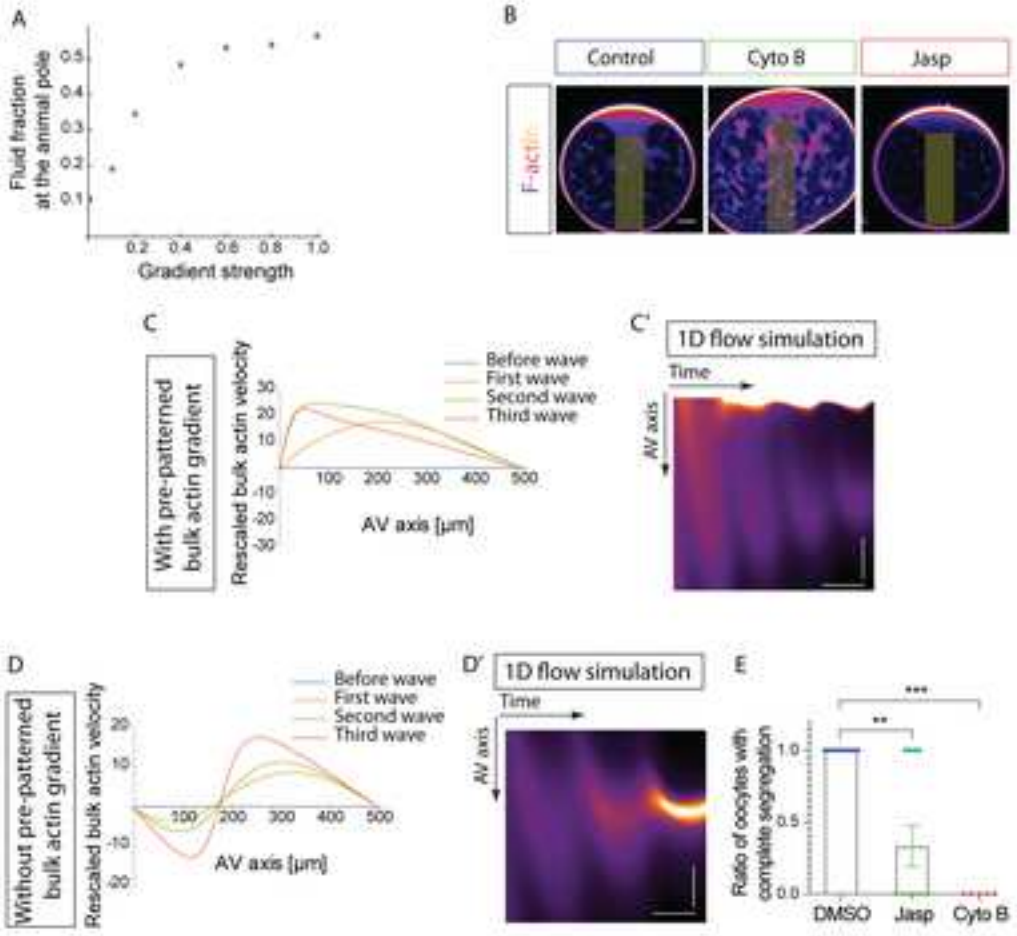

Supp. Figure 7

Click here to access/download;Supplemental Figure;Supfigure2018_7-01.tif